RICE UNIVERSITY

Modeling and Interpretation of Magnetic Flux Leakage

by

David A. Trevino Garcia

A Thesis Submitted
in Partial Fulfillment of the
Requirements for the Degree

Master of Science

Approved, Thesis Committee:

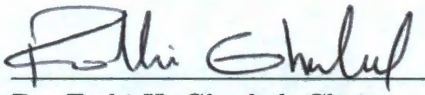

Dr. Fathi H. Ghorbel, Chair
Professor of Mechanical Engineering and
Materials Science

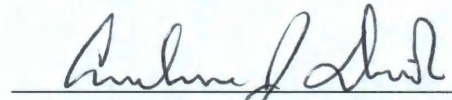

Dr. Andrew J. Dick
Assistant Professor of Mechanical
Engineering and Materials Science

Dr. Beatrice Riviere
Associate Professor of Computational and
Applied Mathematics

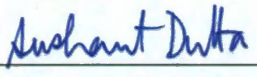

Dr. Sushant M. Dutta
Baker Hughes

Houston, Texas
May, 2012

Abstract

Modeling and Interpretation of Magnetic Flux Leakage

by

David A. Trevino Garcia

This work presents an analysis of Magnetic Flux Leakage (MFL) signal to better understand the forward problem and the physics contributing to the nature of the signals. The analysis of the MFL signal was done through the implementation of two mathematical models such as the Magnetic Dipole Model (MDM) and Finite Element Method (FEM). This thesis shows that MFL signals presents a similar behavior even if the defect's characteristics differ (length, shape and depth). Also, this thesis introudces a Wavelet Analysis (WA) as a tool for further characterization of the MFL signal. This study presents how WA can identify and expose specific characteristics of each defect's MFL signal, even though the signals of different defect shapes were very similar to each other. The main advantage of this work is that it can achieve without changing the current MFL technique, additional information of the defect can be extracted.

Acknowledgements

I would like to express my gratitude to my advisor, Dr. Fathi Ghorbel, who has been more than a guide in this adventure. Also, I would like to thank Dr. Sushant Dutta, whose guidance and support were invaluable to the success of my efforts. I would like to thank the rest of my thesis committee, Dr. Andrew Dick and Dr. Beatrice Riviere, for being helpful throughout the process of the defense. Thanks to my colleagues and friends, Fakhri Landosi, Jaime Taha and Andrew Lynch, for their help and camaraderie throughout.

I dedicate this work to my beloved wife Alexandra who has believed in me without doubts, as well as, to my parents Homero Trevino and Blanca Flor Garcia whose efforts and wisdom have guided me along the right path in life. Finally, thanks to all my family and friends, who have been my pillars of strength through difficult moments of life.

Table of Contents

List of Figures

List of Tables

Chapter 1

Introduction

Cracks have always represented serious threats to the performance of structures in different fields and industries. For many years, people have been studying defects in order to better predict their potential risks and decide if immediate maintenance is required. Several techniques exist to perform on structures a Nondestructive Evaluation (NDE) such as electromagnetic, radiographic, ultrasonic, and thermal. Recently a visual inspection has been introduced in this group of NDE techniques. The NDE techniques have been widely used in pipe inspection field. Typically, most of the pipes used in industries and in the world's cities are ferromagnetic pipes while a small percentage of non-ferromagnetic pipes are most likely used in the private sectors. For industries, pipe line inspections become a very delicate matter because of the economic repercussions that a failure of a pipe could represent for them.

Defects in structures are significant problems for pipeline performance. Nowadays materials such as oil, natural gas, coal, hydrogen, and others are transported using pipelines around the world. Furthermore, this type of transportation started at least 5 decades ago and continued to grow until it became the common way of transportation for energy material types. The importance of keeping pipelines in optimal condition has increased accordingly. Since the steel pipelines became commonly used, steel industry engineers have tried to develop a methodology for reliable defect detection. Therefore, the Robotics and Intelligent Systems (RiSYS) laboratory, from Rice University, has set among their objectives, to develop a pipe inspection technique robust enough not only to detect ferromagnetic defects but to actually characterize the different defects' shapes. Furthermore,

among the different NDE techniques mentioned before, which were also addressed by Bray and Stanley[2] in a technical way, the electromagnetic technique is a promising inspection analysis. The MFL techniques quickly emerged among all the different techniques proposed and became widely used to identify defects location.

1.1 Motivation

It has been almost thirty years from the standardization of the MFL technique and people working in this field have not been able to extract more information from the three MFL signals than the location of the defect along the pipe. That is why such works as Enokizono [3] are very important in this field, in which he tried to solve the inverse problem (defect's shape) by using neural network approximation. Similarly, another work was presented by Frster [4], in which he presented in the mid 80's an early model to find the influence of the defect's geometry on the MFL signals. By now, numerous simulation works have been presented including Yong Li [5], in which by using the FEM computer aided model he tried to characterize different defects. MFL signals were still unknown and the only possible model that was used to compute the MFL signals was the FEM model. But recently, Dutta introduced a model in which by knowing the defect's geometry, it is possible to compute the MFL signals which is known as a forward problem. He also explained how to identify the central axis of a defect by observing one of the components of the MFL signals.

However, still important questions remain unanswered: from a given MFL signal, what is the defect shape? Is it circular? Rectangular? Is it a deep defect? How serious is the defect?, None of these questions can be answered. Therefore, the purpose of this work is to fully describe the dynamics of the MFL signals produced by a ferromagnetic defect and to address how the defects' geometry will determine those MFL signals. Also, another objective of this work is to propose a new approach to extract more information from the MFL signals.

1.2 Problem Definition

In order to analyze the dynamics of the magnetic flux leakage inside defects to characterize the defect topology it is necessary to identify, understand and describe the contributors of the different MFL signals. For example, when a ferromagnetic defect is analyzed, using MFL technique, all measured points are affected in general by all the elements that constituted the defect. Let us consider that P is an arbitrary point in free space near a ferromagnetic defect. Then, if point P is evaluated using the MFL method, there exist some contributors that can affect the measurement at each selected point P. These include:

- Lift-off of the sensors
- Material properties
- Interior defect wall angles
- Dimension of the defect
- Defect's Elements

Moreover, the contribution from each element of the topology of the defect to each point P will be different . In other words, the contribution that one element of the defect surface will make to point P_1 and P_2 will have neither the same magnitude nor the same direction. (Figure 1.1)

This work will focus on a description of how a defect's topology can be represented by applying the MDM and how the MFL signals will emerge from this model. In order to effectively analyze the MFL signals, it is necessary first to understand how the signal is affected by all the contributors and then, to find a way to interpret in an effective manner all the information that the MFL signals contain.

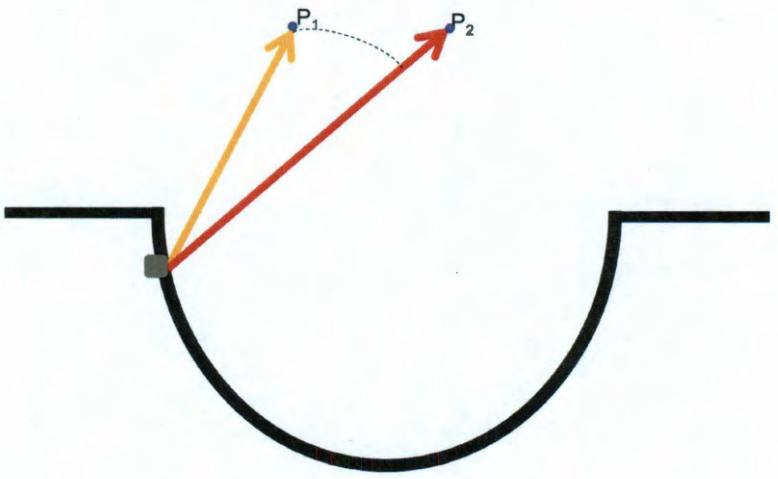

Figure 1.1: Contributions of One Element to Different Point P

1.3 Contributions

The previous section addressed the main challenge of the MFL technique for defect identification. This section identifies the two contributions of this work, that will help to reduce the imperfection of MFL technique.

1. The first contribution of this thesis is to present an analysis of MFL signals to better understand the forward problem and the physics contributing to the nature of the signals through:

   - Mathematical modeling: The Magnetic Dipole Model (MDM).
   - Finite Element Method (FEM).

   This thesis will also explain the dynamics of the MFL signals close to the defect. This will be done through a close analysis using the magnetic dipole model in Chapter Two and the finite element method in Chapter Three .

2. The second contribution of this thesis is to provide an alternative method of interpretation for the MFL signals by using wavelet analysis. This analysis is addressed in Chapter Four.

1.4 Outline of this Thesis

Chapter Two presents the correlation between MFL signals and the respective ferromagnetic defect shape. This correlation is done by applying the mathematical magnetic dipole model. In addition, Chapter Three will present a FEM CAD model used for the development of defect signals of known dimensions. Chapter Four introduces a brief explanation of the wavelet analysis procedure, as well as, the selected mother wavelet function that was applied in this work . Also in Chapter Four, the studied defects will be presented, as well as their full wavelet analysis studies. Finally, Chapter V presents a brief conclusion of this study.

Chapter 2

Magnetic Dipole Model and MFL Signals Description

In the past decades, the MFL inspection method has become the most used technique for pipe inspection around the world. As a result, many people study the MFL technique foundations in order to improve the limitations of this inspection method. For instance, Sung and Rudowicz presented a paper in 2002 [6] in which they addressed the hysteresis loop for ferromagnets and which described the behavior of the magnetization of the materials. In 2003 Mandache and Clapham [7] proposed a model for the computation of the magnetic flux leakage signal in order to predict the MFL signal from a given defect. But this turned out to be only an approximation model of the MFL signal. Great progress has been seen in this field more recently. For decades it was believed that the MFL technique was constituted of only two main components: axial and radial. However, there also exists another ignored signal component which is the tangential component. Dutta made an important contribution to the MFL pipe inspection field in one of his latest publication [8] in which among other important contributions, the third signal component's behavior (tangential MFL signal) was described. He also proposed the MDM for the MFL signals derivation, which was used in this work to explain the behavior of the MFL signal in order to understand the signal's meaning. Also, Dutta described the tangential signal component's behavior at any point P ,where P represents any point located in free space near a ferromagnetic defect's surface. Moreover, he stated that the tangential component will be zero if point P is localized on the defect's axis; in MFL inspection technique the axis will always be parallel to the applied magnetic field. Hence, this contribution gives a great

amount of information about the defect because by analyzing the tangential MFL signal, inspectors can get a sense of the location of the Hall effect sensor with respect to the defect axis. Once that tangential signal was addressed, it was possible to point out the existence of another case in which in the presence of a defect the tangential component will also be equal to zero. Certainly, when an axisymmetric defect is present, the tangential component has to be zero also. The following discussion addresses why the tangential component will become zero in each of the scenarios.

The first scenario where P lies over the defect's axis indicates that the magnetic contribution from both sides of the ferromagnetic defect contributes to point P in an equivalent way but in opposite direction, resulting in canceling each signal (meaning both of the defect's sides will act with the same magnitude to the same point in the opposite direction). The following figure is a 3D schematic of a ferromagnetic cylindrical defect which shows in a top view the MFL contribution from each wall of the defect.

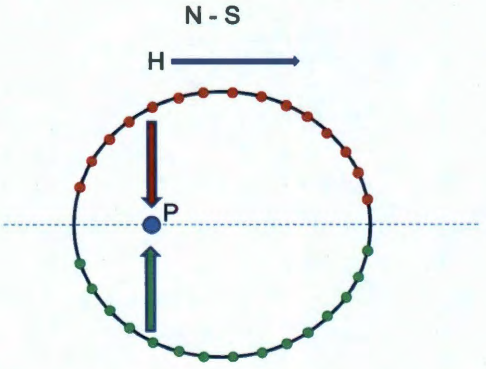

Figure 2.1: Point P Contributors, Cylindrical Defect Top View

The second scenario occurs when an axisymmetric defect is present. This scenario implies the absence of lateral walls (walls in a parallel direction to the applied magnetic field) in the defect. The following figure presents an axisymmetric 3D defect that can be also represented as a defect in a plane that tends to infinity inside or outside the page but without any variation in the defect's shape. Hence, If there are no lateral contributions to

point P, the MFL tangential signal will vanish. The following figure shows a 2D schematic side view of the mentioned defect .

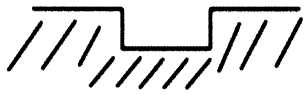

Figure 2.2: 2D Defect Side View.

In order to make a fair comparison between the 3D and 2D models, the second scenario has to be considered. Therefore, from this point on the shown results on this work will also consider the same assumption. Consequently, working in a 2D model and following the previous assumption will reduce the number of MFL signal components, from three signals to two, considering only the axial and radial components for the analysis. This work reduced the number of signals to simplify the explanation, but nevertheless, the knowledge and results that will be presented can be extrapolated to the 3D scenario. In past years, there have been a number of works on the topic of how at any given point P, the MFL signals can be quantified. Accordingly, this work will use the MDM which is a derivation of Maxwell's magnetostatic equations to explain the dynamics of the MFL signal at a given point P caused by the defect's elements.

Maxwell's theory states that if a ferromagnet with a defect is expose to a magnetic field, charge elements will emerge at the defect's surface. Equally important, the theory also suggest that the charge of the element will depend of the normal vector direction of each element of the defect with respect to the external applied magnetic field. An extend discussion regarding this topics will be addressed in section (2.2). The following paragraph will address the mathematical derivation of the proposed MDM.

2.1 Magnetic Dipole Model: Derived from Maxwell's Equations

In this section the formulation of the MDM is presented. Some of the relations that will be mentioned are well known in the magnetostatic field and further references can be found in Halliday and Resnick [9] or any electromagnetics book such as Edminister [10]. Let **B** represent the magnetic field density and **H** the magnetic field intensity. In literature on magnetics it is possible to find that a correlation exists between the magnetic flux density and the magnetic field intensity. Furthermore, **B** will be equivalent to the product of **H** and the magnetic permeability as the following equation presents:

$$\mathbf{B} = \mu_0 \mathbf{H}. \tag{2.1}$$

Maxwell's first equation comes from Gauss's law:

$$\nabla \cdot \mathbf{B} = 0. \tag{2.2}$$

Maxwell's second equation comes from Amperes law, which also contemplates free currents normally represented by **J** in a system. However, MFL inspection technique will not consider any free current in the system. As a result, Maxwell's equation (2.3) will become equation (2.4).

$$\nabla \cdot \mathbf{H} = \mathbf{J}, \tag{2.3}$$

$$\nabla \cdot \mathbf{H} = 0. \tag{2.4}$$

Once Maxwell's equations are recalled, let us assume that a ferromagnetic material is exposed to a magnetic field. The relation between the magnetic field density and magnetic field intensity will be modified. Thus, magnetization usually denoted by **M** has to be included as the following equation presents:

$$\mathbf{B} = \mu_0(\mathbf{M} + \mathbf{H}). \tag{2.5}$$

The general solution of **H** (magnetic field intensity) can be represented as potential energy. Hence, the general solution of **H** can be expressed as the gradient of a scalar potential $\mathbf{v(r)}$ as in equation (2.6). Furthermore, with the previous equations it is possible to compute the magnetic potential inside and outside the ferromagnetic material.

$$\mathbf{H} = - \bigtriangledown \mathbf{V}. \tag{2.6}$$

For example, to compute the magnetic potential that flows inside the ferromagnetic material, equation (2.6) is substituted in equation (2.5) and the outcome is used to replace **B** in equation (2.2) which gives a direct relation between $\bigtriangledown\mathbf{H}$ and $\bigtriangledown\mathbf{M}$ (Equation (2.7)). Thus, $\mathbf{B} = \mu_0(\mathbf{M} + (\text{-}\bigtriangledown\ \mathbf{V}))$, and $\bigtriangledown \cdot (\mu_0(\mathbf{M} + (\text{-}\bigtriangledown\ \mathbf{V}))) = 0$ yield:

$$\bigtriangledown^2 \mathbf{V}_{inside} = \bigtriangledown\mathbf{M}. \tag{2.7}$$

Similarly, to compute the magnetic potential outside the material, equation (2.6) will be substituted in equation (2.1) and the outcome will be used to replace **B** in equation (2.2). The outcome turns out to be $\bigtriangledown^2\ \mathbf{V}_{outside} = 0$, because there will be no magnetization outside the material. With the previous results it is possible to prove that the scalar magnetic potential of any given vector **r** can be written as equation (2.8). The following equation presents the addition of the external applied magnetic field represented by $V_a(r)$ and the magnetization of the ferromagnetic material represented by $V_d(r)$.

$$V(r) = V_a(r) + V_d(r), \tag{2.8}$$

where V_d is composed by 2 integrals, one that represents the magnetic potential of the ferromagnetic material volume and another that represents the scalar magnetic potential at the surface of the ferromagnet defect. The following equation presents the first integral mentioned:

$$V_{d:1st}(r) = \frac{1}{4\pi}\int_{\forall}\frac{-\nabla \cdot M(s)}{|r-s|}d\forall, \tag{2.9}$$

where r represents the location of P and s the location of the defect's element. For MFL pipe inspection, the magnetic permeability of the ferromagnet's elements which are close to the defect is assumed to be constant; more about this assumption was discussed by Bozorth and Chapin [11]. As a result the magnetization vector yields in the following restriction:

$$\nabla \cdot M(s) = 0. \tag{2.10}$$

Hence, the first integral of $V_d(r)$ will vanish. Therefore, $V_d(r)$ will only be composed of the second integral which will yield the following equation:

$$V_d(r) = \frac{1}{4\pi}\int_{s}\frac{n(s)\cdot M(S)}{|r-s|}ds, \tag{2.11}$$

where $\mathbf{n}$ represents the unit normal vector going out of the surface of the defect and $r-s$ represents the distance between a given point of the interior defect's wall and point P. The magnetic field intensity expression generated by the magnetization of the ferromagnet can be achieved by expressing $V_d(r)$ in terms of $H_d(r)$ as equation (2.6) shows. Hence, the magnetic field intensity expression is the following:

$$H = -\frac{1}{4\pi}\int_{s}\frac{n(s)M(s)\hat{\mathbf{j}}\cdot(r-s)}{|r-s|^3}ds(s), \tag{2.12}$$

where $M = M\hat{\mathbf{j}}$, which is nothing but the magnetization of the material expressed in terms of a vector. Now, let us consider dp the magnetic charge of the surface element ds which holds the following relation introduced by Dutta [8]:

$$dp(s) = Mn(s)\cdot\hat{\mathbf{j}}ds(s) = Msin(\theta)ds, \tag{2.13}$$

where θ for a 2D axisymmetric defects analysis will be 90°. Thus the magnetic field intensity variation produced by a defective ferromagnet can be computed by the following

equation:

$$H = -\frac{M}{4\pi}\int_s \frac{(r-s)}{|r-s|^3} ds(s). \tag{2.14}$$

Another consideration used for the derivation of the MDM, it is with reference to the defect's shape. According to Maxwell's theory [12], the defect's shape should be approximated to a second degree polynomial. Maxwell presented the magnetic field's behavior in relation to the defect shape. He proved that for second degree polynomial defect shape the behavior of the magnetic field remains constant within the defect's cavity, while for other shapes the magnetic field will be variable within the defect's cavity. The presence of a variable magnetic field within a defect's cavity will be reflected in the magnetization magnitude that each defect's element will contribute to a given point P. Another point that has to be considered is how the variation of the magnetic field inside the defect's cavity will result in presenting variable magnetic permeability for the material of each element of the defect. The variation of the magnetic permeability of each element can be determined by:

$$(\mu - 1)H = M, \tag{2.15}$$

where μ is the magnetic permeability. Furthermore, it was shown in [13] that an ellipsoid defect shape approximates a second degree polynomial. Therefore, the defect's shape proposed by Dutta for the MDM should also approximate an ellipsoidal cavity. Further explanation and examples were addressed in [8]. Once that relation between the magnetic dipole model and Maxwell's equations was established it becomes possible to address the explanation of how the magnetic charges of the defect's elements determine the MFL signals.

2.2 Magnetic Dipole Model: MFL Signal Contribution

The previous section addressed the derivation of MDM and also addressed how the magnetic field intensity of any point P can be computed using the model. This section will explain how the magnetic charges produced by a magnetic field on a ferromagnetic defect contribute to a point P located in free space. Furthermore, this section will also address how the magnetic charges of the interior walls of the ferromagnet defect and their location with reference to point P will contribute and will also define the magnitudes of the components of the MFL signal. Consider Figure (2.3), which illustrates a lateral view of a rectangular defect at the surface of a ferromagnetic material exposed to a constant magnetic field given by an external source. Let **j** and **k** be considered the unit vectors of the cartesian coordinate system. Furthermore, let the surface of the material without defect be "$k = 0$" and the middle point between both defect's walls be "j $= 0$". The magnetic field travels from north to south and the defect dimensions at this point are assumed to be small compared to the radius of a ferromagnetic pipe. Further description and dimensions of the analyzed defects will be given below.

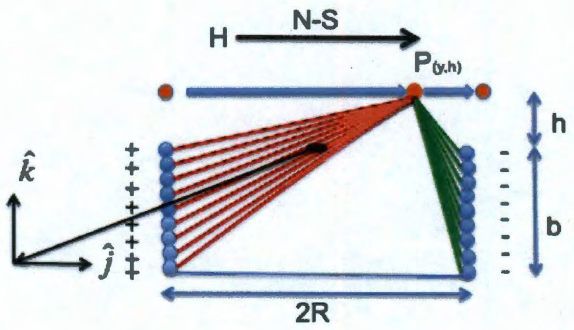

Figure 2.3: Contributors of the Rectangular 2D Defect to Point P

Before the explanation on how the elements of a defect contribute to the MFL signals, the following table presents a set of variables and their definitions.

Table 2.1: Variables Definition

Variable	Definition
O	Origin coordinate system.
P	A given point in space (sensor location).
r	A location of P.
$\vec{r}$	A vector from the origin to a given point P.
y	Axial coordinate of P point. (Horizontal)
h	Lift-off. P point's vertical location. (constant)
s	Given point on defect's surface location.
$\vec{s}$	Vector from a given point on defect's surface to the origin.
v	Axial coordinate of the charge point on the surface.
z	Radial coordinate of the defect's surface. (Vertical)
$\vec{q}$	The distance difference between a given defect surface's element and P point. (|r-s|)
M	Magnetization
b	Depth of the defect.(constant)
R	Half of the defect length. (constant)

Figure (2.4) shows a schematic of a defect using the adopted notation, where each blue square represents an element of the charged wall. However, at the bottom of the defect it is possible to observe an absence of charged elements because that plane is parallel to the magnetization direction. The magnetic dipole model was derived from the first principle of Maxwell's equations. Maxwell stated that there will be no charged elements in surfaces that form a perpendicular normal vector to the magnetization direction. Therefore, the derivation of Maxwell's equation leads to the following distribution: charged elements along the defect's surface if the element's normal vector does not form a 90 degree angle with the magnetization direction (external applied magnetic field).

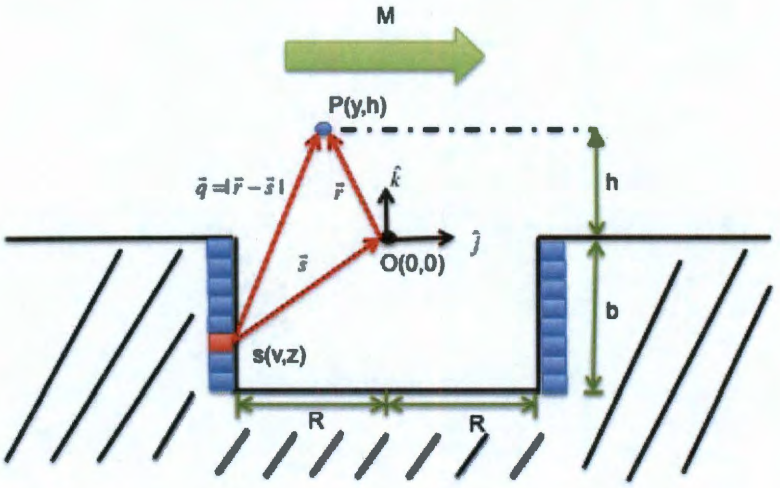

Figure 2.4: Identification of Variables- Rectangular Defect

Similarly, the charge of each element will entirely depend on the surface plane angle with respect to the magnetization direction. For instance, the following figure will introduce the distribution of the charged elements as well as the normal vector direction of each plane of the rectangular defect presented previously.

Each element's magnetic charge will be defined by their normal vector's direction. If the direction favors the magnetization direction, the elements will present a positive charge while elements with a normal vector direction opposing the magnetization direction will

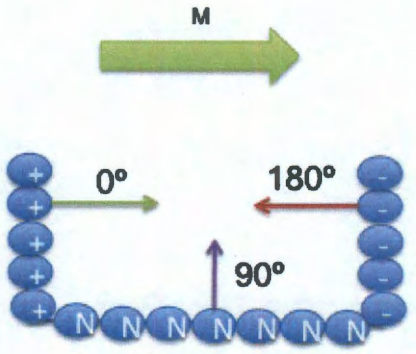

Figure 2.5: Element's Normal Vector Direction of a Rectangular Defect

present a negative charge. Also, the previous figure shows how at the defect's surface, locations where the normal vectors are perpendicular to the magnetization direction will not present any charge. Having addressed how to identify the elements of the defect and how to define the charge of the elements, it is possible to address how the charge elements will behave. Let equation (2.14) be rewritten in the following form by using the introduced notation:

$$H_{\pm}(r) = \frac{M}{4\pi} \int_S^0 \frac{q\hat{\mathbf{j}} + q\hat{\mathbf{k}}}{q^3} dS. \tag{2.16}$$

The term $|r-s|$ which represents the distance between a defect's element and P point is substituted by q. Also, the numerator is separated by components because equation (2.14) can be also separated by components. Similarly, this previous equation can be expressed in a coordinate system (Figure (2.6)), in which it will be easier to understand and visualize the location of each defect's charged element:

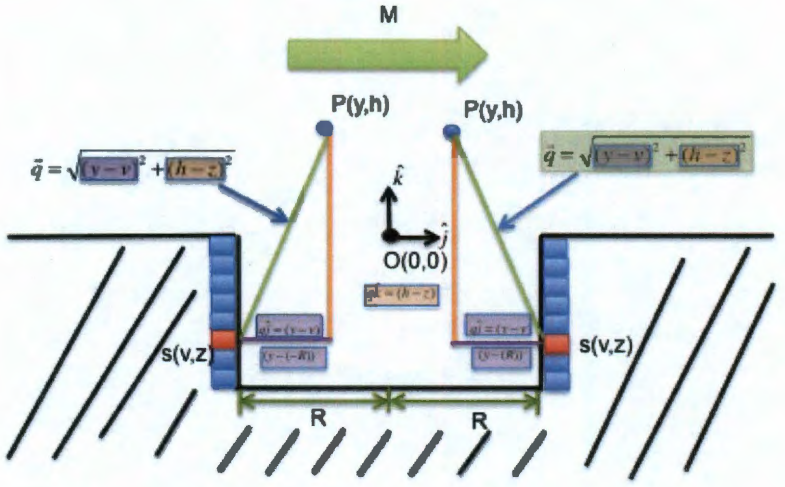

Figure 2.6: Rectangular Defect's MFL Radial Signal

The coordinate system expression will be as the following equation shows:

$$H(z) = \frac{M}{4\pi} \int_{-b}^{0} \frac{(y-v)\hat{\mathbf{j}} + (h-z)\hat{\mathbf{k}}}{((y-v)^2 + (h-z)^2)^{3/2}} dz. \tag{2.17}$$

From the previous figure it is possible to conclude that the axial contribution from a charged element will be given by the axial distance between the element and P point divided by the magnitude of the distance between the element and P point elevated to the third power. In a similar way, to compute the radial contribution from a charge element to P point, that will be given by the radial distance between the element and P point divided by the magnitude of the distance between the element and P point elevated to the third power. To illustrate this, let the following rectangular defect example clarify the previous statement. In the previous Figure (2.6), each element of each wall has its own coordinate and v can take the values of "$-R$" and "R" for each respective side wall while "z" will be the integral's variable. Before addressing MFL signal descriptions for this defect it is important to understand how the magnetic dipole model computes each signal. The model's integral will consider the location of each defect's element with respect to the "P" point location, in order to compute the vertical and horizontal distance between

them and then compute the resultant distance as well. For instance, once the horizontal (axial) and vertical (radial) distances between one element and "P" are divided by the resultant distance elevated to the 3th power, those values multiplied by the magnetization of the element over 4π will represent the axial and radial contribution from that particular element to the desired point "P". Therefore, to compute the axial and radial values of "P", the previous procedure has to be applied to all the elements which constituted this defect and then the results have to be included in a summation. The magnetic dipole model will do the previous procedure without using a summation. The following figure shows all the vectors that have to be considered to compute the magnetic field at a given "P" point.

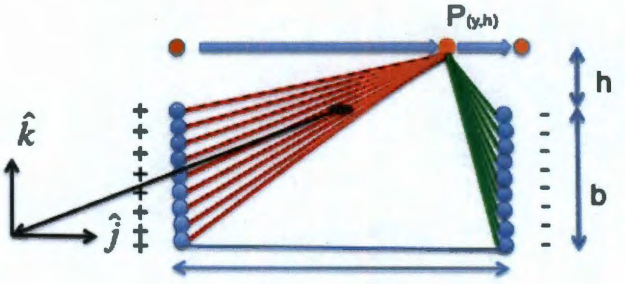

Figure 2.7: Considered Vector Contributors for a Rectangular Defect

Per Maxwell's theory, the behavior of the elements will not be the same for any point in space. From the analysis of the polarity of the charges it is possible to conclude that the behavior of each element will depend on three factors:

1. Magnetization field direction.

2. The element's magnetic charge.

3. The location of the element with respect to point P.

By taking into consideration the previous factors it is possible to represent the behavior of the charge elements as presented in the next table:

Table 2.2: Element's Behavior Maps

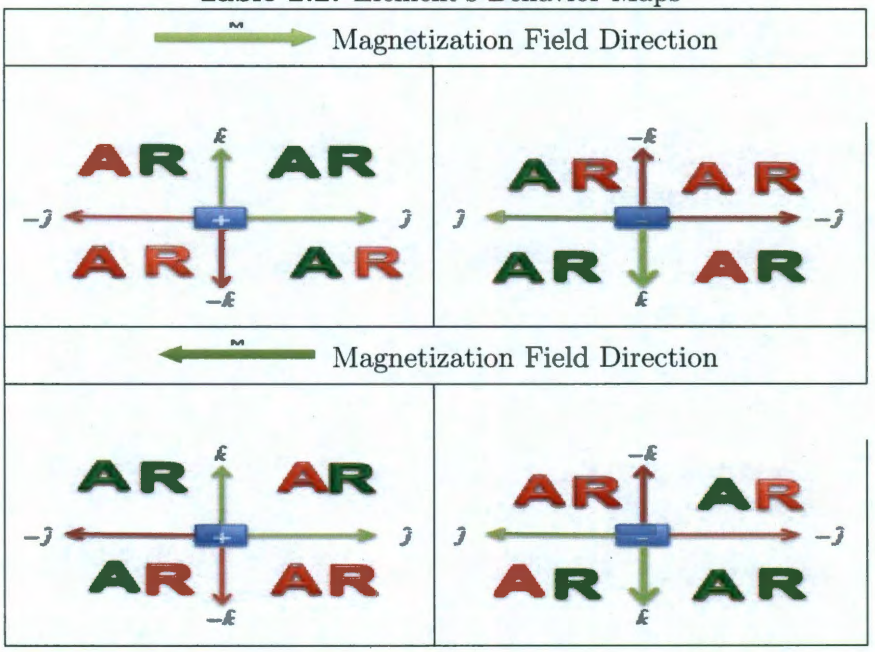

where "A" and "R" represent the Axial and Radial MFL contribution respectively. The green color represents positive contribution and the red color represents negative contribution from the element. Now it is possible to analyze the contribution from the elements at a given defect shape. For instance the following figure shows the defect's element contributions over a "P" point.

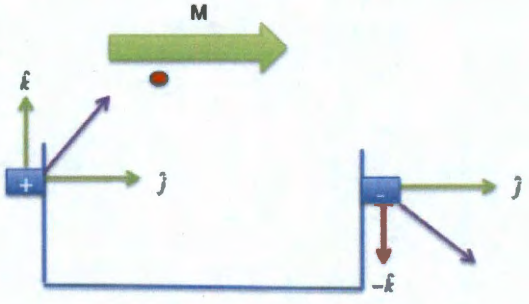

Figure 2.8: Element's Behavior Dependent On the Charge.

This section has already discussed how the magnitude of the contribution from each element can be determined but the behavior of each element for a given point P can be anticipated by using the element's behavior map just mentioned. Equally important, for this proposed rectangular defect, when point P is located outside the defect's range, the closest wall's elements will contribute to the axial component in a negative way while the radial contribution will not be modified without affecting the axial location of point P (Assuming that P is located at some positive lift-off). For instance, let us consider a positive charged element at some random location in a defect and also let us consider the magnetization directions as the following figure shows. Then, if point P is located in the first cartesian plane with respect to the charged element, such as $P1$ at some coordinate $(+j, +k)$, the positive charged element will contribute in a positive way to the axial and radial components of $P1$. If however point P is located in the second cartesian plane with respect to the charge element, such as point $P2$ at some coordinate $(-j, +k)$, then the contribution from that element over point $P2$ will be positive in the radial sense, but negative in the axial sense.

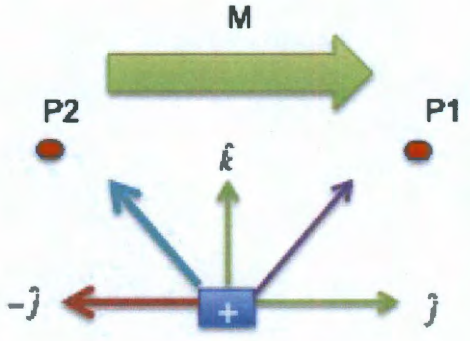

Figure 2.9: Element's Behavior Positive Charged Element.

One important point that this work has not yet addressed is the importance of lift-off. It is extremely important to understand that every element's contribution to points P will be bounded by the distance among them as was established before. Therefore,

lift-off distance has a very important role for MFL signals computations. If the lift-off is small, the distances between the elements and the position of the sensor will be reflected on the MFL signal, but the higher the lift-off is, the more similar the contribution from the elements over a point P will be. In fact, equation (2.14) and (2.17) are composed by the fraction $\frac{1}{|r-s|^3}$ and $\frac{1}{|q|^3}$ respectively which is nothing but one over the distance between wall's elements and P to the power of three. Therefore the following plot will present the relation between $|q|$ and $\frac{1}{|q|^3}$.

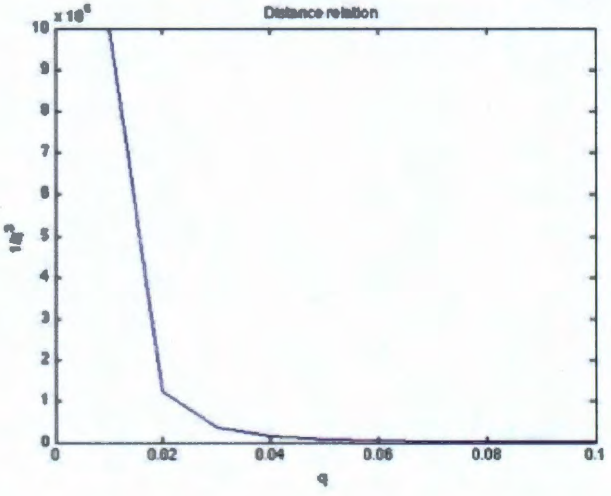

Figure 2.10: q vs. $1/q^3$ Distance Relation

This relation emphasizes how the element's contribution depends on the distance. It is possible to conclude form the previous figure that the closer an element is to point P the higher the contribution from that element over point P will be. Another way to interpret this relation is that for higher lift-off distances, the contributions will be smaller from all these elements over P. Also, the wall's bottom elements will tend to contribute less to P as lift-off increases. Likewise, Figure(2.10) emphasizes the importance of the constant lift-off magnitude during any experiment, in order to avoid undesired variation in the MFL signals readings. A brief comparison of MFL signal outcomes using different lift-offs will be presented in section (2.4). The following section presents an explanation of the meaning

of MFL signals. This analysis was done by using different ideal defects' geometries.

2.3 MFL Signals Description

This section will present an analysis of different defect geometries in order to address the MFL signal interpretations with references to each defects' geometry. Once the contributors are identified in a defect and the way of contribution is explained, it is possible to understand the MFL signal behaviors. For instance, for all the defects that this work will present, the defects' dimensions were the following: $6mm$ of defect length and $3mm$ of maximum depth. The following figure will present the radial MFL signal computed for the rectangular's defect.

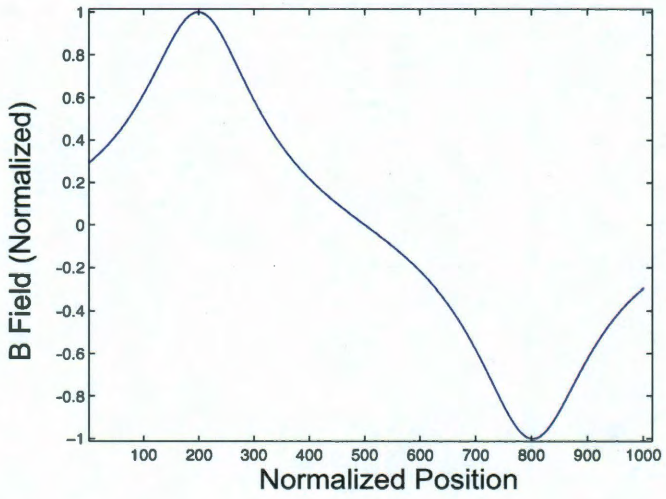

Figure 2.11: Rectangular Defect's MFL Radial Signal

Figure (2.11) shows the normalized radial signal of the rectangular defect where the positive and negative defect's edges are at 200 and 800 respectively. The contribution from each element to the final magnitude of "P" will not be determined only by the distance between the points, since the polarity of each element will determine if the element contributes in a positive or negative manner to "P". For instance, there are few observable

characteristics that can be expected from the radial signal of a rectangular (symmetric) defect.

1. Maximum and minimum points of the radial signal should be above the defect's edges (200 & 800).

2. The MFL radial signal should be zero at the origin of the coordinate system (0,0).

In order to explain the first point, recall equation (2.17), in which it is possible to observe that the distance magnitude between "P" and each wall's element will be at the denominator elevated to the 3th power. Also, the vertical (radial) distances between each couple of points (P & each wall's element) will be the nominator of the integral which will always be smaller than the distance magnitude (denominator) with one exception: when P is above the edges, in that case they will have the same magnitude but different exponents. Thus, the nominator presents an exponent 1 while the denominator has an exponent of 3. Therefore, the ratio between the nominator and its denominator will keep decreasing as the distance between each couple of points keeps increasing. As a result, the contribution from an element over point P decreases as the distance between the points increases. In the MFL technique the sensor will tend to pass over the defect length at a constant lift-off, meaning that it computes the MFL's values of "P" at different locations over the defect but with a constant radial position. Thus, for the rectangular defect the smaller distances between the elements of one wall and a point P on path P will be when the location of point "P" is exactly above the defect's edge. Therefore, that location of P will receive the maximum contribution from all those elements of that defect's wall. Another observation can be made from this defect shape. Let P be above one defect's edges and elements from the opposite wall will still contribute in an opposite direction to the radial signal, but because the distance between those elements and "P" will be very high compared to the distance between the elements of the closest wall to "P", the opposite wall's element contributions will be very small in comparison. The second point can be addressed by observing figure (2.7). Let "P" be at coordinates $(0, h)$. Then, for each

red line which represents the contribution from the elements of some negative magnitude there will be a green line of the same positive magnitude. Thus, the contribution from the positive charge elements and the negative charge elements will be identical but with opposite signs. Therefore, adding all the elements contribution will mean that they cancel each other. This is a typical behavior of a symmetric defect for the radial signal.

The axial signal can be analyzed in a similar way. The following figure will present the axial signal of this rectangular defect.

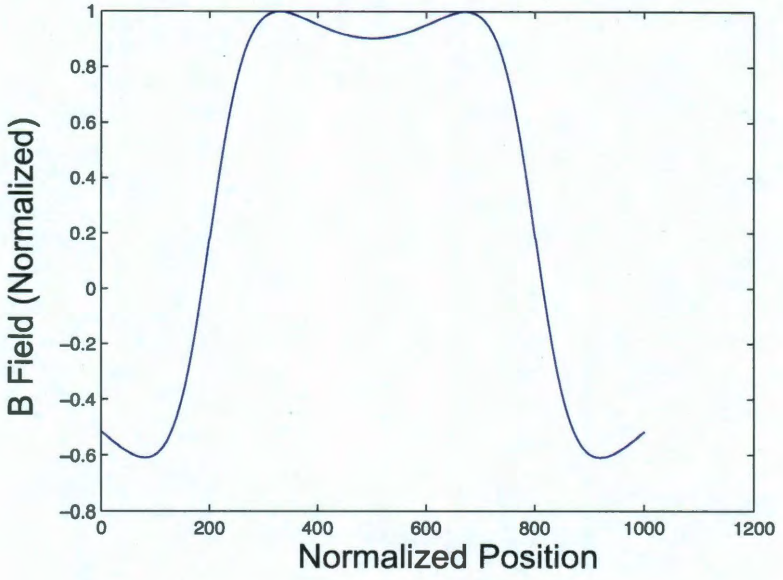

Figure 2.12: Rectangular Defect's MFL Axial Signal.

As in figure (2.11), in figure (2.12) both edges are located at (200 & 800). Contrary to what happens at the MFL radial signal computation, at the axial signal, every element of the defect contributes in a positive way over "P" points, which are located between the defect's edges. This can be proven by analyzing the behavior of each charge element using the behavior maps presented in the previous section.

Finally, once the element contributions' behavior has been established, the axial signal explanation can be addressed. Typically, the axial signal of symmetric defects presents

the maximum point exactly midway between both edges (500 location in Figure (2.10)). However, the signal distribution is explained before. The distance between each element of each wall to a given point "P" will determine the final magnitude of "P". For instance, for this rectangular defect, the length between the defect's walls is very high. High distances between the edges will be reflected in the contribution over points "P" closer to the defect's center. Therefore, it is possible to interpret the center signal curvature of Figure (2.12) as an absence of contribution from the elements of the defect. Normally, in pipeline inspections, defects' dimensions are not high and this previous atypical signal's behavior described will not be commonly observed.

In a similar way, this section will also present an analysis of other geometries. Other geometries have a similar analysis. The following table introduces the four defects that were analyzed and compared for this work.

Table 2.3: Four Defect Geometries

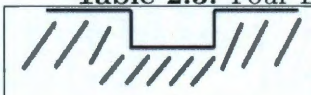	Rectangular Defect
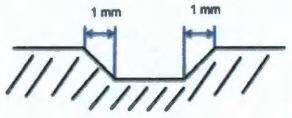	Trapezoid Defect 1
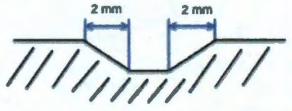	Trapezoid Defect 2
	Notch Defect

The length between the beginning and end of each defect shape at the pipe's surface ($k = 0$) will be the same $6mm$. The maximum depth will be also the same for every defect $3mm$. The three added shapes present lateral walls with angles. The dimension of the variable zones can be observed in the previous table. The first analysis will be for trapezoid defect. The variable zones at this defect are of $1mm$ at each side of the defect's

shape. As an illustration of how the MFL signals can be computed by using the MDM, the following figure presents how the variation of the lateral wall can be computed to include those variations at the MDM.

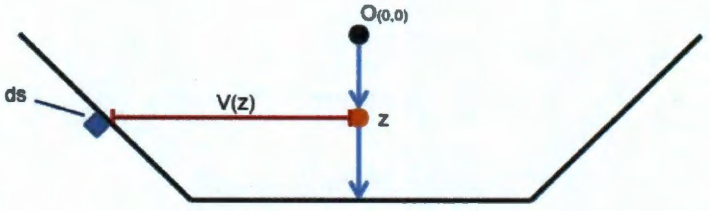

Figure 2.13: Defect with a Variable Wall Angle.

Note that "v" ,which is a variable, will be a dependent of "z" the variable of the integral and radial coordinate of each wall's element. Now, another representation of equation (2.17) will be introduced. Each wall's element can be located by using the wall's angle and the radial "z" parameter. The following figure presents this case.

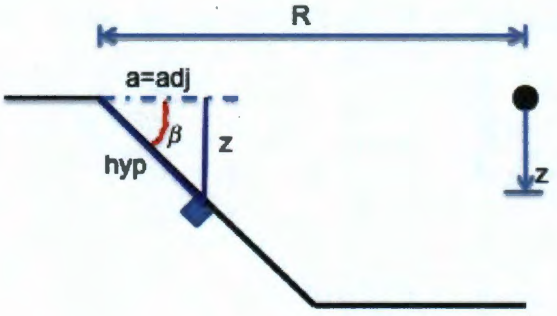

Figure 2.14: Variable Wall as Function of β Angle.

For any given "z" length, there will be a element with a coordinate $(v(z), z)$. As an illustration, the following equations explain how to compute "v" by using the β angle. Let β be $0 \leq \beta \leq 90$, then:

$$\sin\beta = \frac{z}{hyp},$$

$$hyp = \frac{z}{\sin\beta},$$

$$a = (hyp)\cos\beta,$$

$$a = (\frac{z}{\sin\beta})\cos\beta,$$

$$a = z\cot\beta.$$

Thus, by computing the adjacent length of the rectangular triangle in figure (2.14), it will be possible to compute "v".

$$v = \pm(R - a) \tag{2.18}$$

The sign of "v" will be determined by the location of "v" with respect to the origin of the defect. With this new relation, equation (2.17) can also compute the magnetic field intensity of a defect with linearly variable walls. The magnetization "**M**" of each element will be also constant, because all the wall's elements present the same normal vector angle with respect to the external magnetization field. Once the explanation of how to compute "v" variable with a given angle has been determined, the radial signal for the first trapezoid defect can be presented as follows.

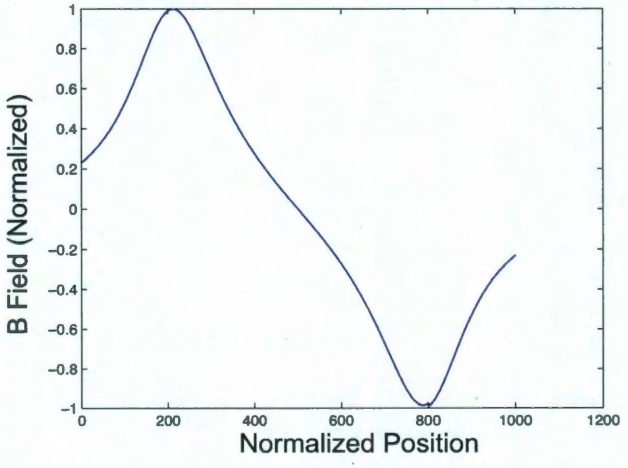

Figure 2.15: Trapezoid One Defect's MFL Radial Signal.

From the foregoing figure it is possible to make the following observations:

1. It is possible to observe a thinner curvature near the maximum and minimum points.

2. The curvatures that appeared at figure (2.11) between the maximum point and the middle point and between the middle point and the minimum point tended to disappear. This occurred because the location of the defect's elements were closer to "P" points which are closer to the center of the defect.

The first point can be explained from different points of view. For instance, a defect with a 90 degree angle at the edge produces a higher concentration of MFL near the edge. After all, the smaller sets of distances between every element of a wall and "P", will occur when "P" is located before and after each edge. Equally evident, if the defect's wall presents an angle smaller than 90 degrees, this will produce a higher contribution over "P" when "P" is located within a defect's edges and less contribution to "P" outside the defect's range. In other words, when the wall's angle is less than 90 degrees, points "P" before and after the defect length will receive less contribution from the closest wall. Now the second point can be also explained. Likewise, the aforementioned curves that appeared in figure (2.11) occurred because there exist a lack of contributions from the defect's elements as a result of the high distances between the elements and the points P closer to the center of the defect. On the contrary, for this trapezoid defect, all the defect's elements closer to the bottom will make higher contribution to points "P" near the defect's center and less contribution to points P near the edges in comparison with the previous defect shape. This has occurred because the distance among the elements and points "P" closer to the center will be drastically reduced with the introduction of angle β to both defect's walls. The fallowing figure presents such a scenario.

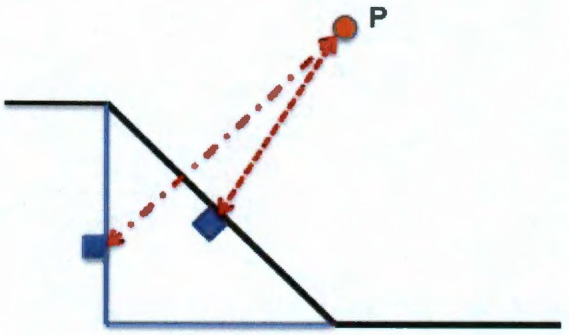

Figure 2.16: Position of P with Respect to Different Elements

Similar to the way the radial signal was analyzed, the MFL axial signal will be presented. The following figure shows the MFL axial signal for the first trapezoid defect shape.

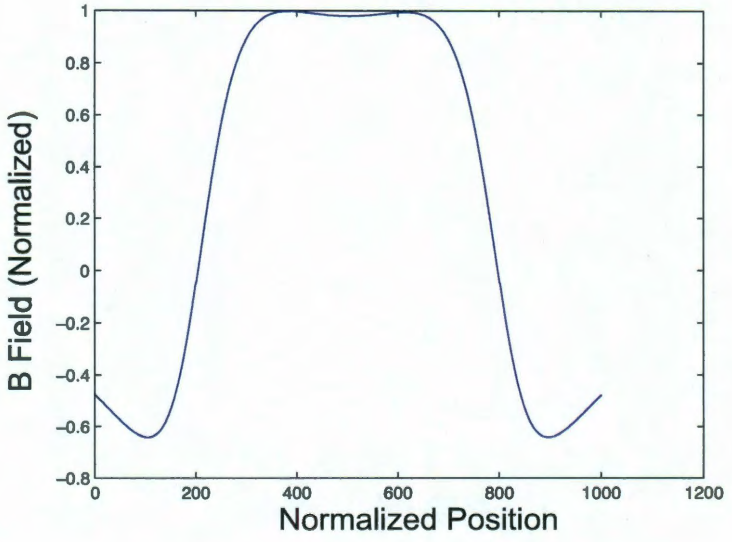

Figure 2.17: Trapezoid Defect One: Defect's MFL Axial Signal.

Evidently, the lack of contributions that appeared closer to the center of the MFL axial of the rectangular signal tended to vanish from the defect shape's signal presented in Figure (2.17). Furthermore, the maximum point of the axial signal did not occur at the

defect's center and again, it was possible to observe two maximum points in the signal. Also, one remark that was not pointed out before, it was mentioned that every element of the defect will contribute in a positive way to "P" located in within the range of the rectangular defect, but defect shapes with variable walls were not discussed. Therefore, elements of the defect's wall will contribute in a positive way for some P points and in a negative way for other locations. This can be anticipated by analyzing the defect's shape with the behavior map of the charged elements. Similarly to how the previous defect's shape was analyzed, when the location of P is outside the defect's range the behavior of the elements will be as follows: all elements of the closest wall will contribute to the axial signal in a negative way to "P" points which are located near the edge but outside the defect's range. In contrast, elements of the farthest defect's wall,will contribute in a positive way to points P located outside the defect range but on the opposite side of the defect.

Of course, the previous scenario occurred because is an ideal defect and all the positive elements are located at one side of the defect and all the negative elements are located in the other side of the defect. Now assume that one of the defect shapes has an imperfection in the positive side wall and because of the imperfection, a negative charged element emerges in the wall. The negative charged element will contribute in an opposite form than the behaviors of the positive charged elements. The behavior of this element will affect all the points P located inside and outside the defect's range. With this scenario presented, let us return to the analysis of ideal defect shapes. Another characteristic of the trapezoid defect's signal is that it is also possible to observe that wall elements of the trapezoid defect shape will contribute less to points "P" outside a defect's length because the distance length between them will be higher, due to the angle of the wall. As a result, signal values outside the defect's range should tend to be smaller. It is also possible to observe how the closest wall's elements will contribute in a negative way if the elements were analyzed by using the behavior maps. Also expected is how as the angle of the defects' wall (β) keeps decreasing, the range of P points outside the defect range which will

be affected will keep decreasing.

In like manner, the second trapezoid defect shape can be analyzed. This second trapezoid defect will have a higher variable length at each defect side. Thus, this variation will result in charged elements closer to points "P" near the system origin (defect's center). Also, the variation of the angle will also be reflected in an increment of all the distances between the defect's elements and "P" points outside the defect's range. The following figure presents a schematic of the location of the elements at both trapezoidal defect's shapes.

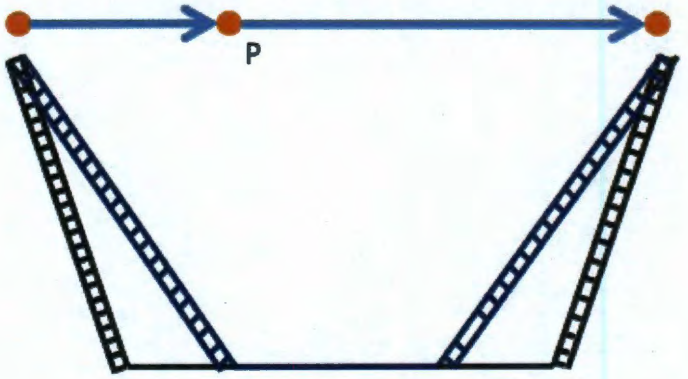

Figure 2.18: Charged Element Locations for Trapezoid Defect 1 and 2.

From the previous figure it is possible to observe why the second trapezoid defect's angle will produce a higher contribution to points "P" within the defect's range. The variable axial length for the second trapezoid defect's shape will be $2mm$ per side as can be observed in table (2.3). The following figure introduces the MFL radial signal.

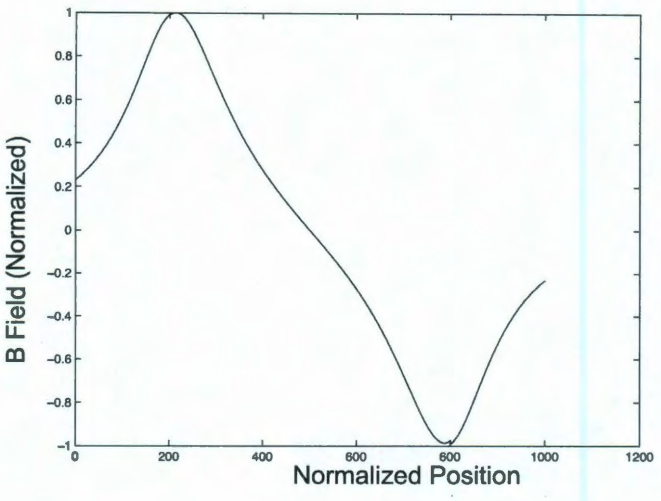

Figure 2.19: Trapezoid Two: Defect's MFL Radial Signal.

From the previous figure, it is possible to conclude that "P" points within the defect's edges and the defect's center did receive a higher contribution than at previous analyzed defects. In other words, it is possible to observe almost a straight line between maximum and minimum points of the signal, which means that both curves between the defect's edges pointed out, before in the previous signal's analysis as a lack of contribution, have tended to disappear in this analysis. It is also possible to observe how the location of the maximum and minimum point are not at the edges of the defect (points 200 and 800). This occurs because the overall distances between the defect's elements and points "P" inside the defect become smaller than the overall distances of elements to a point "P" located above the start of the edge. Therefore, as the wall's angles keep decreasing, the maximum and minimum points will continue moving towards the defects' center. The following figure presents the axial signal of this defect and in the same way, the signal can be analyzed.

Logically, the maximum point appeared at the center of the signal as expected. Also, it is possible to observe how the first and last value of the signal were closer to zero magnitude than the first and last value of the previous two analyzed defects. The following study

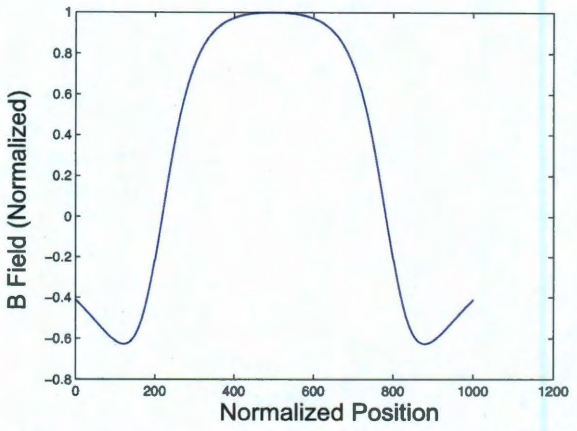

Figure 2.20: Trapezoid Two: Defect's MFL Axial Signal.

presents the notch defect MFL signal analysis, which should continue with the tendencies presented by the previous defects. The following figure shows the MFL radial signal.

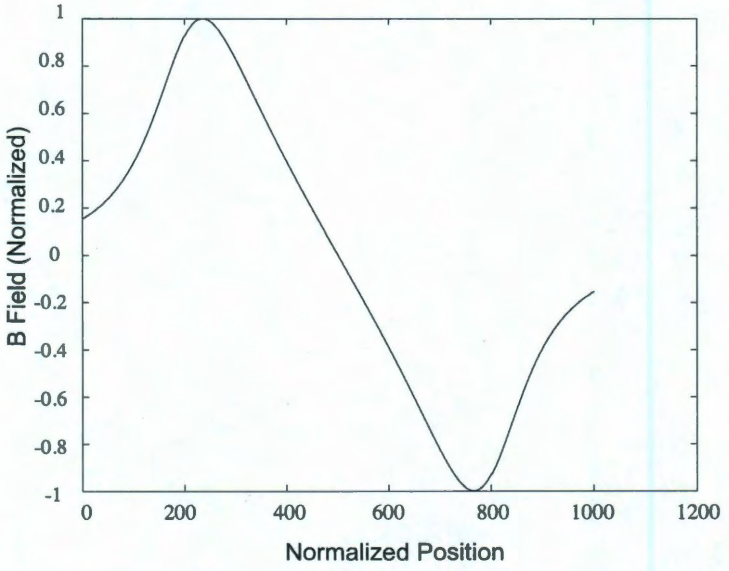

Figure 2.21: Notch Defect's MFL Radial Signal.

It is anticipated that radial MFL signal will present a straight line between maximum and minimum points. However, this has occurred because of the dimensions proposed for this defect shape. For different dimensions, the signal will present different behavior. For

instance, let b (depth of the defect) be $1mm$ instead of $3mm$, and "P" points within defect's range will receive a higher MFL contribution as a result of the short distances between the defect's elements and P path. Hence, this example will result in curves opposite to the one presented before. To illustrate the following figure presents the MFL radial signal for the notch defect with a maximum depth of $1mm$.

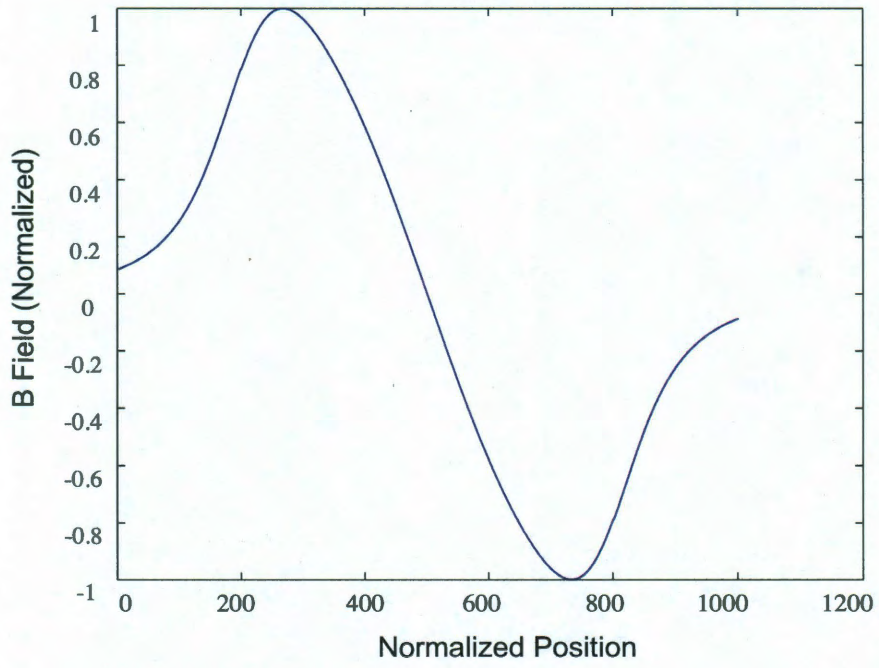

Figure 2.22: Notch Defect's MFL Radial Signal- Example ($1mm$) Depth.

Evidently, in the previous figure it is possible to observe how the location of the maximum and minimum points were clearly far from the actual edges. Also, the signal presents curvatures between the defect's edges, which indicates high contributions from defect's elements. After this brief example, the axial signal of the original notch defect can now be introduced. The following figure shows the MFL axial signal.

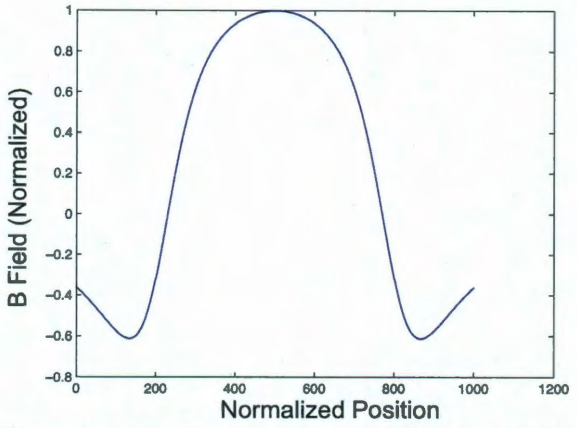

Figure 2.23: Notch Defect's MFL Axial Signal.

In the previous figure, It is possible to observe a more defined signal closer to the center of the defect. Hence, it indicates the location of the maximum point. In order to compare all the defects' results in an effective way the following figure presents a summary of all the radial signals presented on this work. This will simplify the comparison between the signals.

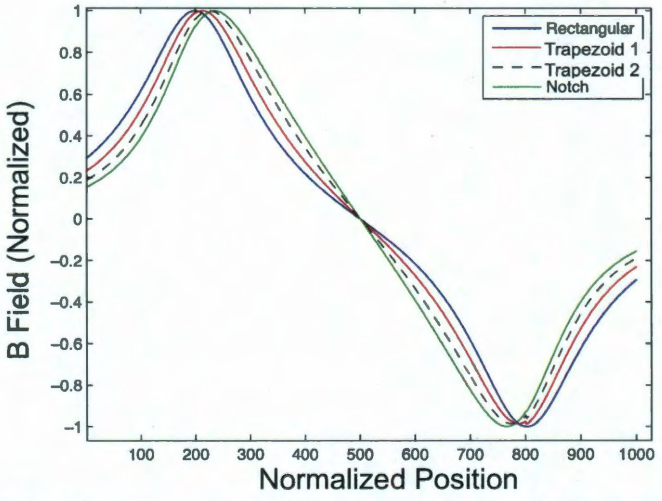

Figure 2.24: Summary of all Analyzed Defects - MFL Radial Signal.

The previous figure shows the following relation: as the angles of the walls are getting smaller, the maximum and minimum points of the signal tends to move to the signal's

center. Also, the location of the wall's bottom elements result to be crucial for "P" points near the system's origin, which receive higher contribution when the angle β become smaller. This can be observed at the curves before mentioned. Similarly, the following figure presents a summary of the axial MFL signals.

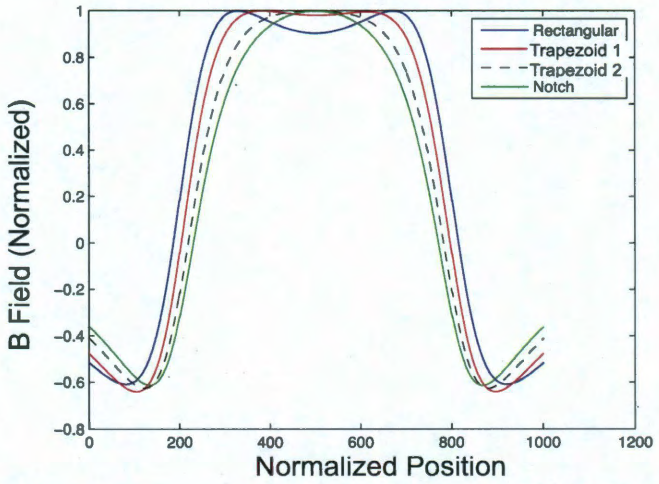

Figure 2.25: Summary of all Analyzed Defects - MFL Axial Signal.

Consequently, the previous figure shows that for "P" points near the origin, as the wall's elements got closer, their magnitude increased. Another remark to be made about the previous figure, is the magnitude difference of the beginnings and the ends of the signal obtained with different wall's angle. Without doubt, the MFL signals have a direct connection with the defect geometries. Of course as the complexity of the defect's shape increases, the interpretation of the signal tend to be more difficult. Also, some of the analyzed axial signals presented a lack of contribution near the center of the signal. This could have been avoided by using a smaller lift-off. The following section will address how the lift-off can affect in a direct way the readings of the Hall effect sensor of the MFL robot.

2.4 Lift-off: Contributor and Determinants of the MFL Signals.

This section will present a study of the MFL signals produced by the four different shapes, in order to show that bigger lift-offs produce different MFL signals. This fact can result in a misleading interpretation of the defect's shape. Therefore, for all the experiments, the dimensions used were the following: $6mm$ of defect length between lateral walls and $3mm$ of maximum depth, and this study did not consider "P" points outside the defects' range. The following tables will introduce the different MFL normalized signals produced by each defect using different lift-off. Every aspect of the experiment remained the same, and the only difference among the signals was the lift-off.

The first table will present the rectangular defect results. The second and third tables present the trapezoid defects results respectively while the last table of this section presents the results of the notch defect. It will be possible to observe how as the lift-off grows the MFL signals tend to be very similar among them.

After analyzing the previous tables, it is possible to conclude that lift-offs higher than $1mm$ will result in a misleading signal and the extracted information will not be enough to make further characterization of the defect's signal. This chapter concludes after analyzing the different contributors of the MFL signals. Also, this chapter explained how the different contributors will be reflected on the MFL signals. The following chapter will briefly present a FEM model and solutions of the four different defects analyzed. It is important to include the FEM analysis because as was addressed before, for the MDM analysis the magnetization of the defect's elements were assumed to be constant. Furthermore, the FEM analysis will indicate if the constant magnetization used for this model should be considered as a constant or a variable.

Table 2.4: Rectangular Defect MFL Signals for Different Lift-Off

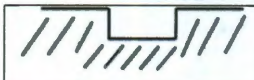	Radial Signal	Axial Signal
Lift-Off 1 mm	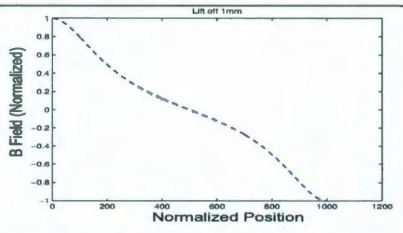	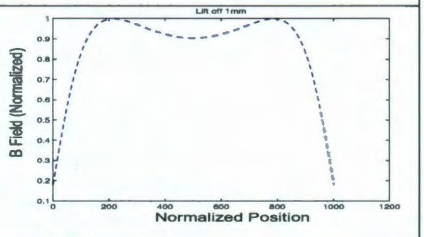
Lift-Off 2 mm	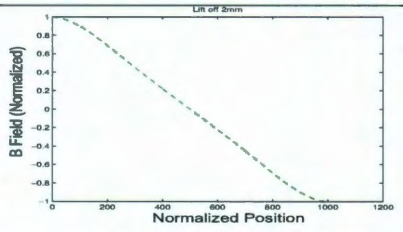	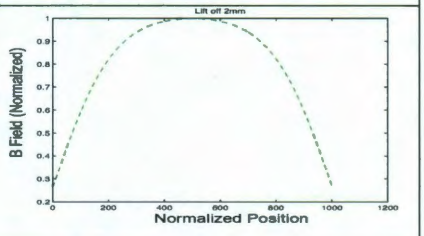
Lift-Off 3 mm	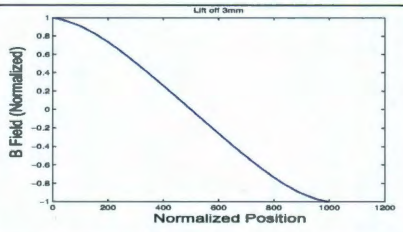	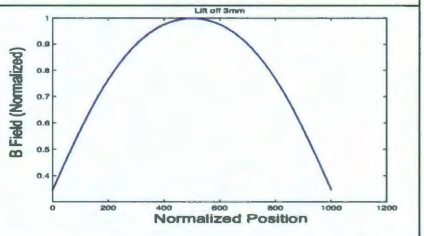
Lift-Off 4 mm	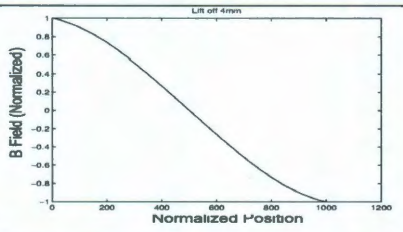	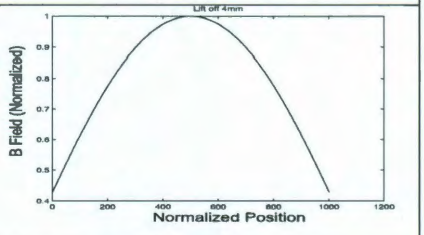
Lift-Off 5 mm	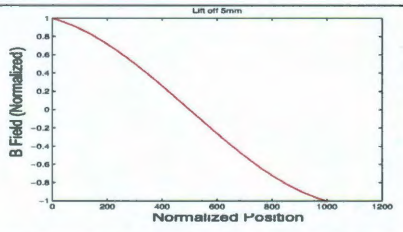	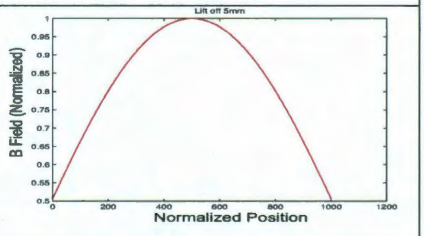
Summary	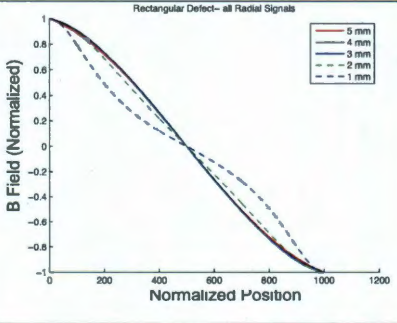	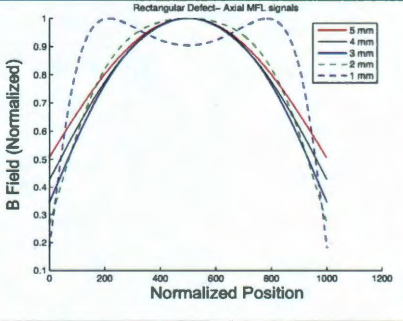

Table 2.5: Trapezoid Defect 1 MFL Signals for Different Lift-Off

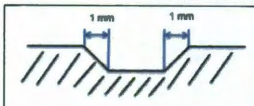	Radial Signal	Axial Signal
Lift-Off 1 mm	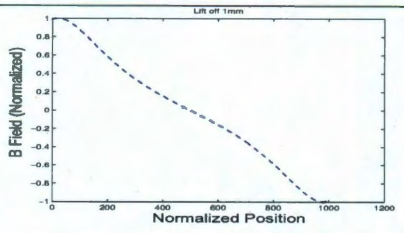	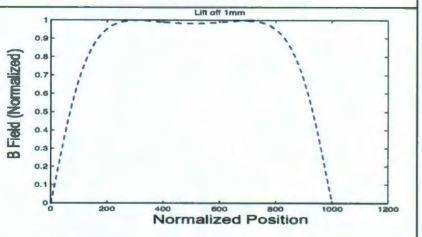
Lift-Off 2 mm	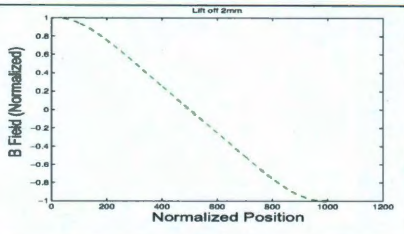	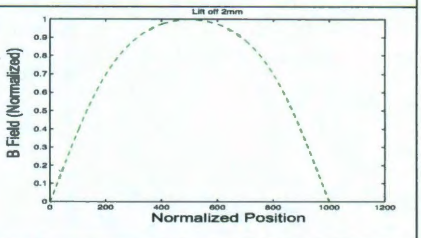
Lift-Off 3 mm	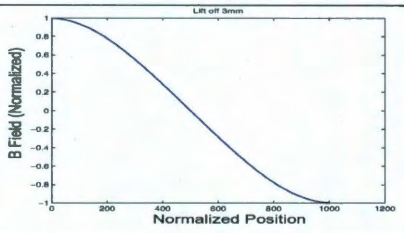	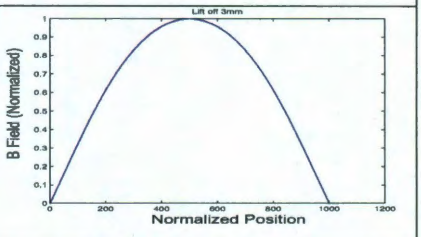
Lift-Off 4 mm	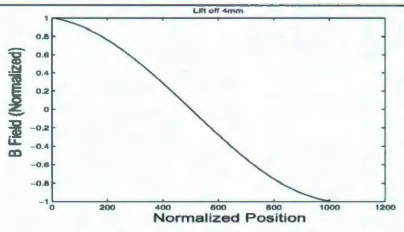	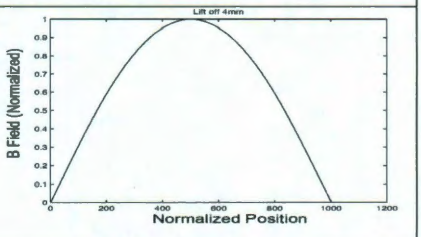
Lift-Off 5 mm	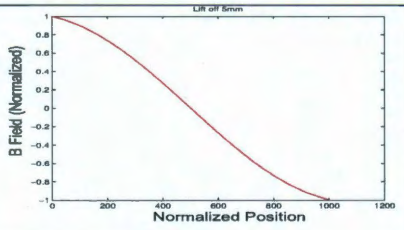	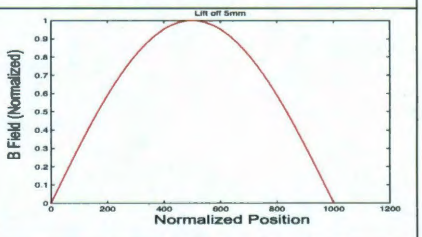
Summary	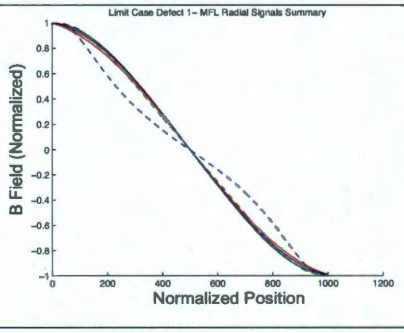	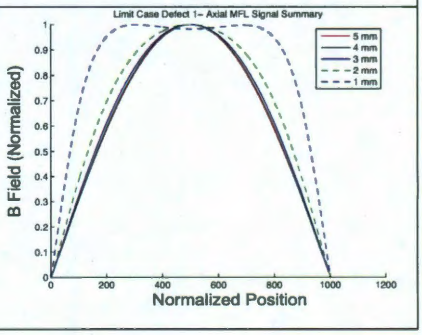

Table 2.6: Trapezoid Defect 2 MFL Signals for Different Lift-Off

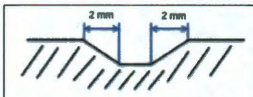	Radial Signal	Axial Signal
Lift-Off 1 mm	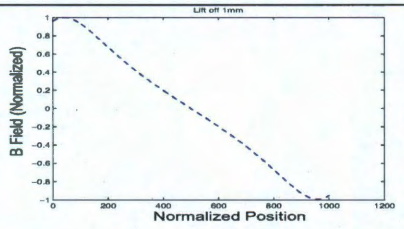	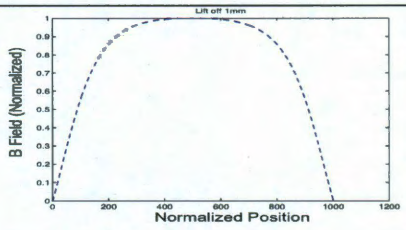
Lift-Off 2 mm	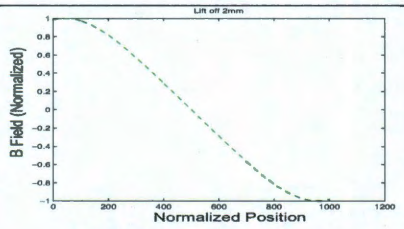	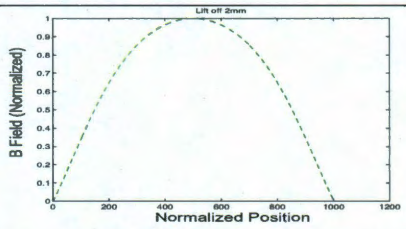
Lift-Off 3 mm	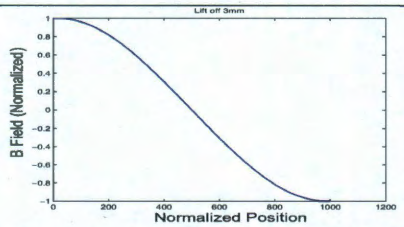	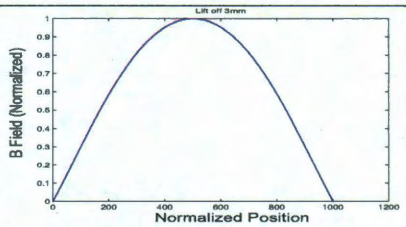
Lift-Off 4 mm	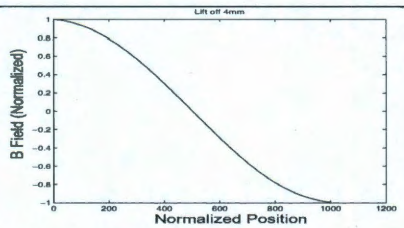	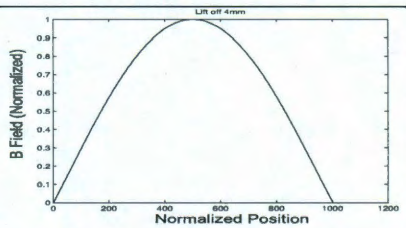
Lift-Off 5 mm	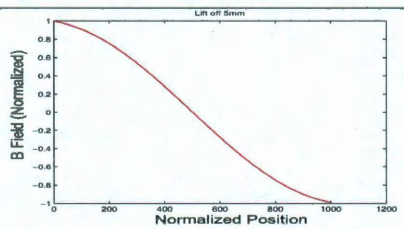	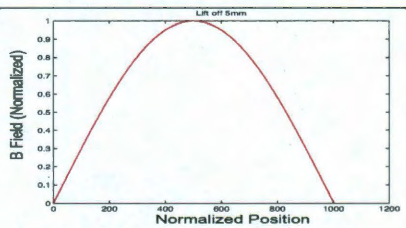
Summary	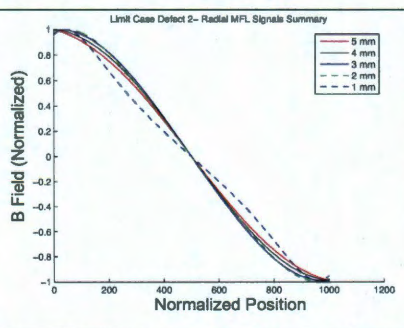	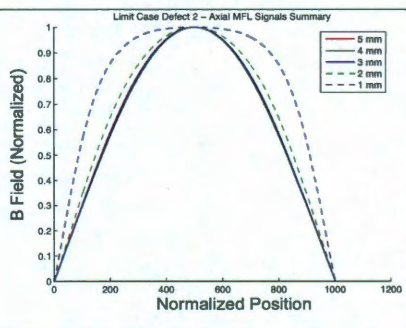

Table 2.7: Notch Defect - MFL Signals for Different Lift-Off

	Radial Signal	Axial Signal
Lift-Off 1 mm	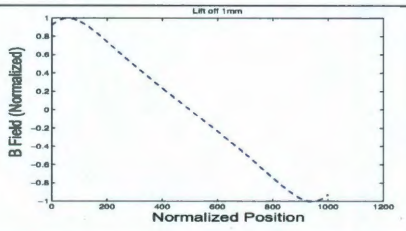	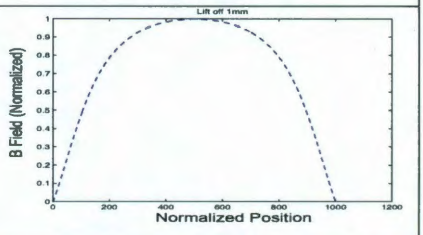
Lift-Off 2 mm	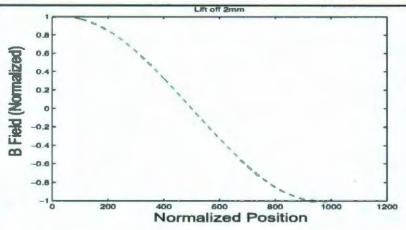	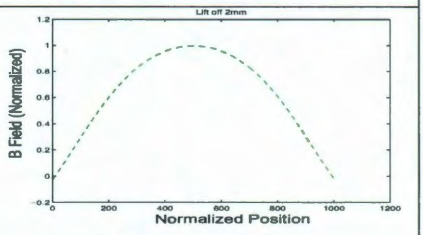
Lift-Off 3 mm	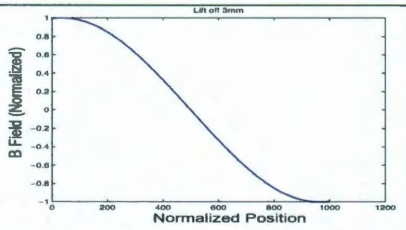	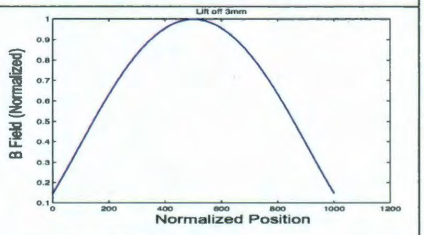
Lift-Off 4 mm	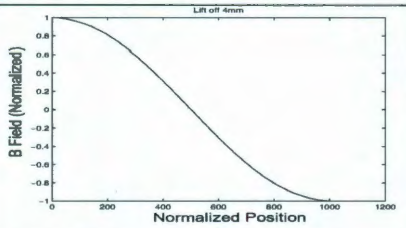	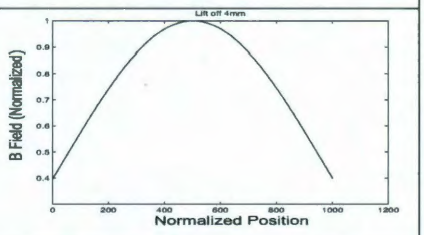
Lift-Off 5 mm	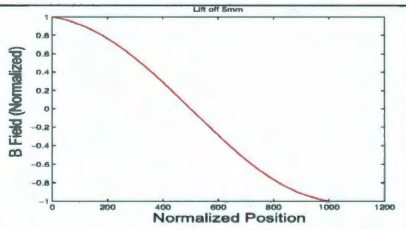	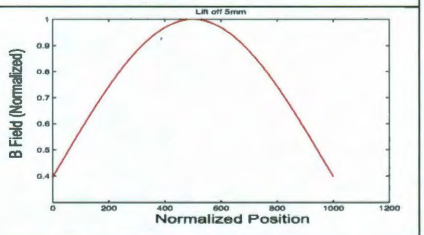
Summary	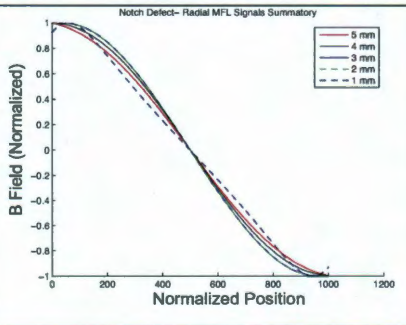	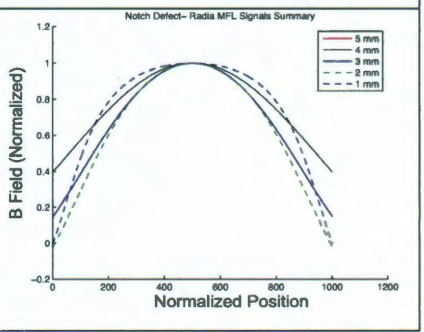

Chapter 3

MFL and Finite Element Method

Finite element method (FEM) has been successfully used in different branches of science for the past four decades, where theoretical and practical problem solutions have been found by using FEM. The FEM can be also applied to MFL systems if the computer software aims to solve Maxwell's equations. Another advantage that FEM method has with respect to other approximation methods is that contrary to other methods such as Finite Difference, FEM can dramatically increase the accuracy of a problem's approximation solution. Thus, in the present work, FEM was used to analyzed different ferromagnetic defects' geometries, in order to extract the MFL signal's outcomes. For CAD construction and finite element analysis with magnetic field solver capabilities, an ANSYS computer package was used.

The same four different defect shapes analyzed in the previous chapter were studied in this chapter, in order to corroborate the extracted MFL signals computed by the MDM. In addition, the lift-off, which is the distance between the original pipe surface and the sensor, was the same for all the exercises in this chapter ($1mm$). Further experiments were performed with different lift-offs. The codes to obtain those results will be included in the appendix (A,B and C) of this thesis.

3.1 Background of FEM Analysis in MFL

Finite element methods have been used many times for MFL simulations in which by solving Maxwell's equations, the nonlinear problem can be numerically solved. FEM method was not very popular before the 80's when computers technology limitations were holding down this powerful method, of course that finite element method computations has

changed in the last couple of decades at the same rate that technology capabilities have been improved. But even with hardware limitations, before the 80's there were a few publications in this field such as Hwang and Lord [14] in 1975 when they published a FEM model of the magnetic field around a ferromagnetic defect. That work could be consider as a pioneer of a FEM model for MFL cases even though their model was very limited because of hardware. Twelve years later, Atherton et al presented two works in which they applied FEM to approximate the solutions to the proposed problems. The two works were the following:

1. "Finite Element Calculations on the Effects of Permeability Variation on Magnetic Flux Leakage Signals" presented with Czura [15] in which they showed the effects of different permeability of the ferromagnetic material in a MFL problem.

2. "Finite Element Calculation of Magnetic Flux Leakage Detector Signals" with Daly [16], in which they studied different variables of the MFL to improve the MFL sensing system.

Without doubt these works did represent more demanding computation work in the numerous elements used for the analysis. As a result of the increment of elements in the analysis the accuracy of the solution drastically improved. From that point on, FEM has represented a highly accurate tool for MFL field. Therefore, computer FEM software packages have included sections for magnetic field science which can manage and solve this type of problems. In 2003 T.C. Roberts [17] presented a simulation in which he modeled an MFL test bed created by Tulsa University. Furthermore, he showed how the Hall effect sensors collected the signals and how the simulation produced similar results. Five years later Wyatt Chase Breidenthal [18] from the same university also modeled an axisymmetric ferromagnetic defect in ANSYS and also did experimental work using the same test bed. These two works had great relevance to the work that this thesis presents because similar

FEM simulations and similar experimental work were done. However, Roberts and Breidenthal have presented a comparison between a 3D physical problem, such as extracted information from the analyzed axisymmetric defects performed in the test bed, and a 2D axisymmetric FEM computer simulation, but the 3D analyzed defects were machined. As a result, a machined defect could present imperfections not only at the defect's surface but also at the interior of the pipe's wall which could produce a different MFL signal. Thus, variations from the simulations and the real MFL signals could exist. Therefore, ideal defect shapes were studied in this thesis as in the previous works, but in order to avoid the previous problems the FEM signals were compared with the extracted MFL signals of the magnetic dipole model (MDM) which can reproduce signals of ideal defects as well as imperfect ones.

Similarly in 2008 Dutta [8] proposed some FEM models to analyze defects signals in a more detailed form. Different software packages were used in Dutta's work as a corroboration method. Also, Dutta described how by solving Maxwell's equations, FEM could be used to solve the MFL nonlinear problem.

This work will propose a similar model than the one presented by Bridenthal to analyze different defect shapes. The proposed model for this work will not consider temperature variations or other external factors that could affect an experimental recompilation of information. Of course, the model that Bridenthal proposed represents the test bed that the University of Tulsa developed. The model that this work proposes will take into consideration the simplest test bed with a coil that surrounds the pipe. More details about this model will be addressed in the following section.

3.2 Description of MFL Finite Element System

Robotics and Intelligent Systems (RiSYS) laboratory developed a pipe inspection testbed (PIT) which uses the MFL methodology. Furthermore, the PIT robot is conformed by two coils which follow Helmholtz coil specifications, leading to a constant magnetic field at the position halfway between both coils. In addition, PIT robot has one Hall effect sensor localized midway between both coils where the magnetic field is uniform. This sensor detects the MFL magnitude of the three components of the signal (axial,radial, and tangential). More about PIT specifications is addressed by Andrew Lynch at his Masters thesis[19]. When a pipe is being analyzed by PIT, the pipe and PIT share the same axial axis. As an illustration, the following figure, part (A), will present a 3D schematic of the PIT robot and the pipe. The PIT robot was designed to analyze one line slice of the exterior wall of a pipe, which can be interpreted as a slice of the wall of the pipe. A slice of the pipe wall and of the coil can be observed at the next figure part (B) which is a 2D representation of the axisymmetric cad observed at part (A).

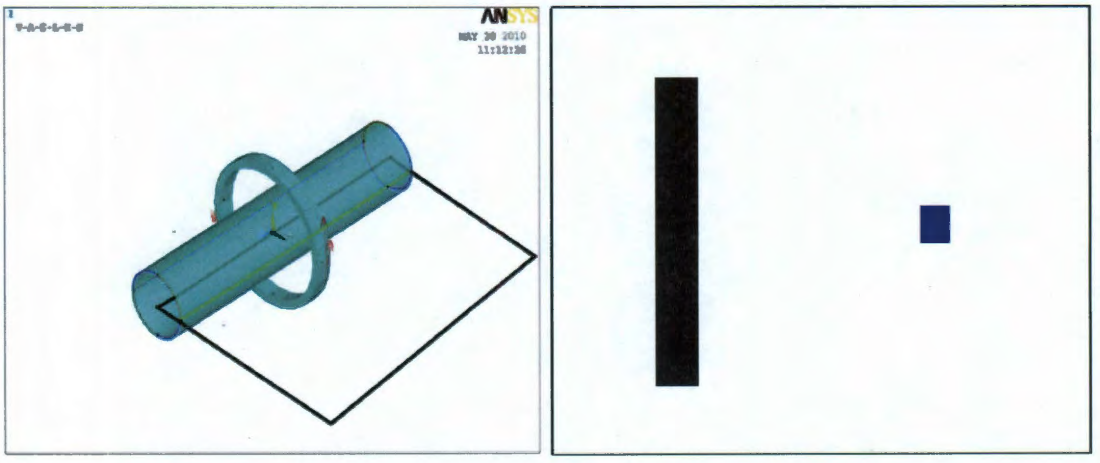

Figure 3.1: FEM Model A) 3D System Schematic B) 2D System Schematic

Moreover, if an axisymmetric defect (defect that revolves 360 degrees) is present at the surface of the pipe, it can be sketched in 2D as the following figure shows. An illustration

of this type of defect would be a wall thickness reduction or an increment of thickness of the pipe's walls, where both scenarios could be considered as an axisymmetric pipe defect.

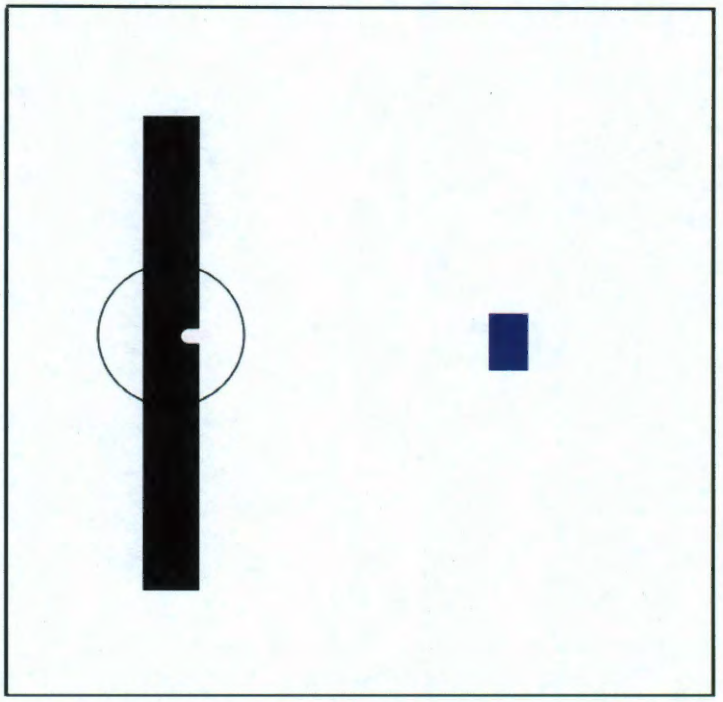

Figure 3.2: 2D System Scheme with a Defect

Having discussed the translation from the 3D physical problem to the 2D analysis scenario, let's recall the four studied cases that were shown in the previous chapter. The same four shapes were studied by using finite element method. The following tables presents the defect's shapes and the extracted MFL signals (axial and radial) from the FE model as well as the ANSYS displayed solution of FEM models. All the extracted signals in table 3.2 show only the defect's range signal. Also, the defect's edges will be located at points (0 & 1000) and the center of the defects at point (500).

Magnetic flux leakage signal components will present the following behavior. The MFL axial signal's magnitude will be very high compared to the radial signal, and this will happen because the established MFL axial component's direction will parallel the external magnetic field direction. Nevertheless, the signals that will be presented were normalized for comparison purpose. Also, as addressed in the previous chapter, the axial MFL signal will be composed by the defect element's contributions depending on the reference location of the element with respect to point P and the system characteristics addressed in the previous chapter. Therefore, as described before, for the MFL axial signal, every element of the defect will always contribute to the movement of the flux leakage excepting those elements located below the point P (same axial and radial axis). After having analyzed the axial signals shown in the following table, the answer to the question of why the axial signal analysis will not give much information about the defect's characteristics will be easier to visualize. Even though, along all the defect's length, the MFL axial signals have greater magnitude than in the rest of analyzed space and could give a hint of the defect's length, the change of MFL magnitudes closer to the defect's edges could mislead analysis to a wrong interpretation of the defect's edge location. After all, the axial signal will be a projection of the wall angle and if there isn't any information about the lift-off distance, it will be impossible to predict the defect's edges. Contrary to the axial signals's results, the radial signal can actually point out where the edges are localized, and that with the MFL magnitude before and after the edge could be used to understand the defect's geometry involving different lift-offs within a defined range.

Table 3.1: Four Defects - Finite Element Analysis MFL Displayed Solution

Rectangular Defect		Trapezoid Defect 1	
Radial Signal	Axial Signal	Radial Signal	Axial Signal
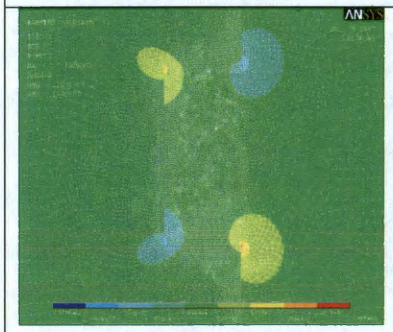	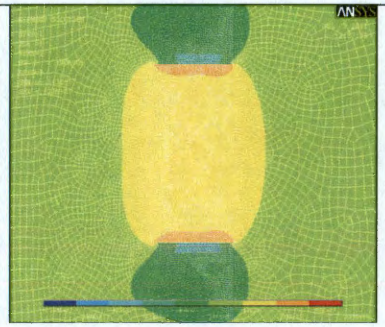	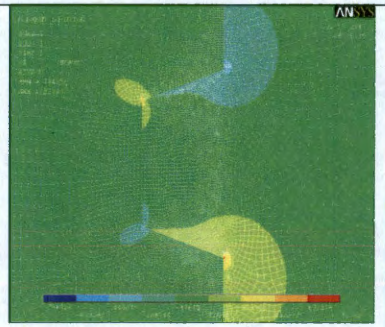	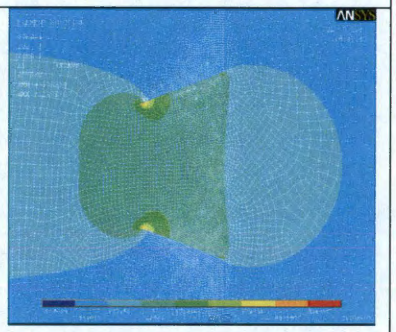
Trapezoid Defect 2		**Notch Defect**	
Radial Signal	Axial Signal	Radial Signal	Axial Signal
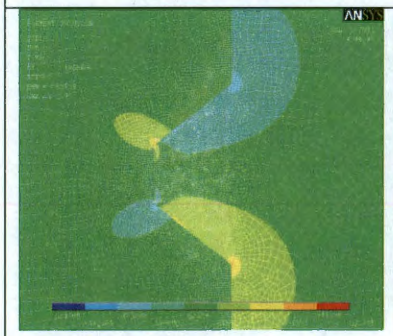	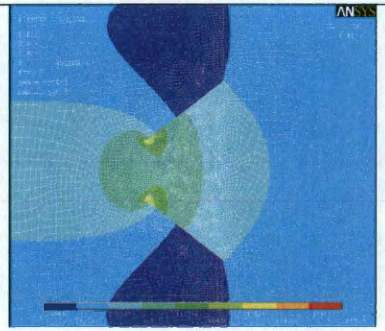	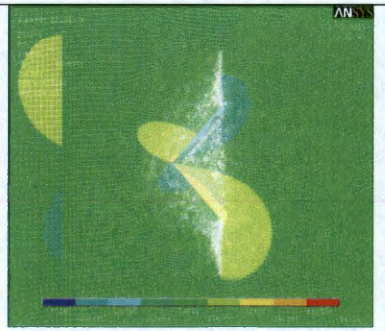	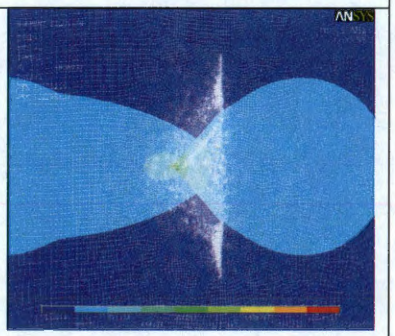

Table 3.2: Four Defects - Finite Element Analysis MFL Extracted Signal

Rectangular Defect		Trapezoid Defect 1	
Radial Signal	Axial Signal	Radial Signal	Axial Signal
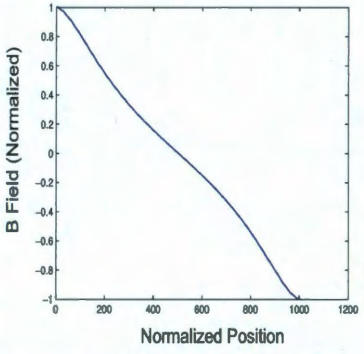	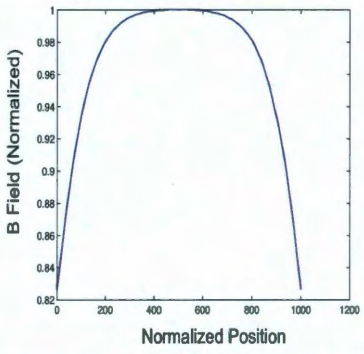	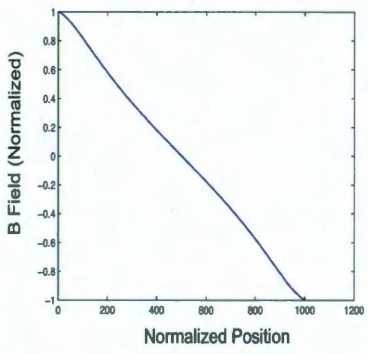	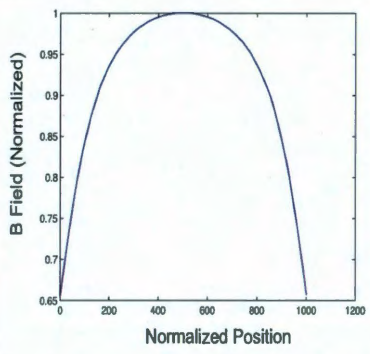
Trapezoid Defect 2		**Notch Defect**	
Radial Signal	Axial Signal	Radial Signal	Axial Signal
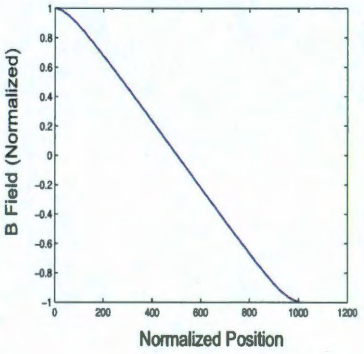	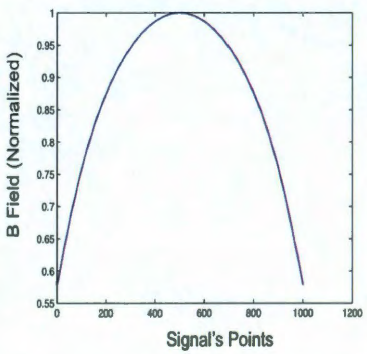	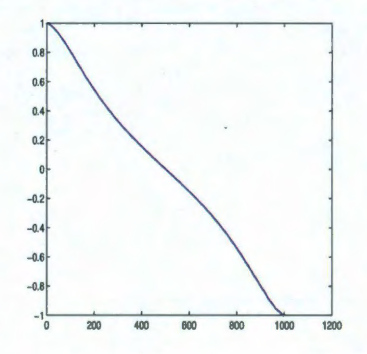	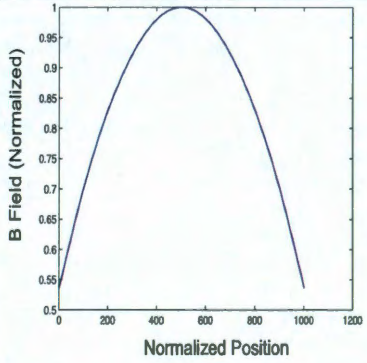

The FEM system having been explained and its purpose and capabilities discussed, the following section presents the accuracy of the magnetic dipole model with reference to the FEM system.

3.3 FEM MFL Signals Vs. Magnetic Dipole Model Signals

This section will compare the FEM model's solutions against the MDM's solutions. There exist different aspects that have to be considered before performing this comparison. For instance, some parameters that cannot be entirely controlled in the FEM analysis, such as mesh symmetrically. In some FEM simulations, the required element's dimensions in a mesh can not be a achieved because of hardware limitations. On the other hand, the MDM proposed by Dutta entails a few assumptions which could cause small differences. Therefore, the following table shows the comparison outcome. It is possible to observe that the approximation of both methods turns out to be very similar, but only for some of the analysis.

The element dimensions that were used for the FEM analysis near the defect area were of the same length as the those elements used at the MDM analysis. Also, in each FEM model, the boundary conditions have to be carefully selected and imposed in order to avoid undesired variation in the solution. Therefore, for all MFL performed simulations the magnetic field was selected to be zero when free space domain reached 4 meters away from the pipe axis (which represents a big free space area on the simulation with respect to the selected pipe's and coil's dimensions). Consequently, the dimensions of the mesh's elements used in this study did not were uniform because of equipment limitation. The following figures present the final mesh for one of the studied defect's shapes.

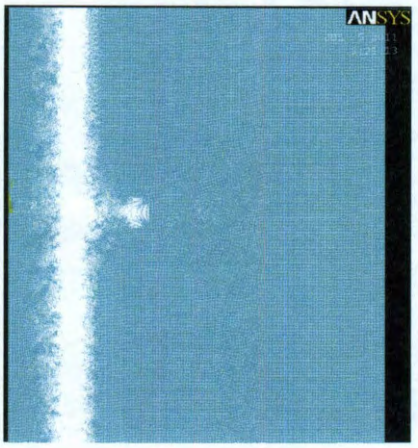

Figure 3.3: Final Element Mesh - Rectangular Defect

A closer look at the defect area is shown in the following figure.

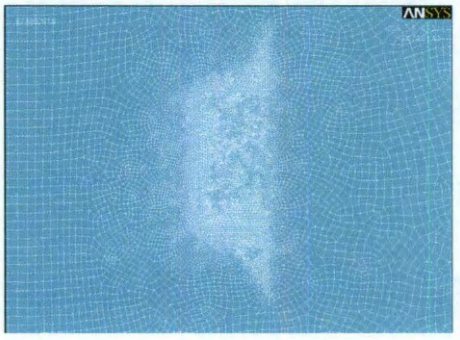

Figure 3.4: Final Element Mesh - Rectangular Defect Close Up

Finite element method was used in this work as a corroboration source for the MDM. Likewise, the FEM analysis model was used as MFL signal source for the wavelet analysis chapter instead of using the real MFL signals which were extracted from the RiSYS robot. As a result, the accuracy of defects shape and the absence of signals noise were the two factors that were controlled by using the MFL signals from the FEM model. The following table presents a comparison between the FEM extracted signals and the MDM extracted signals.

Table 3.3: Four Defects - Finite Element Analysis MFL Extracted Signal

Rectangular Defect		Trapezoid Defect 1	
Radial Signal	Axial Signal	Radial Signal	Axial Signal
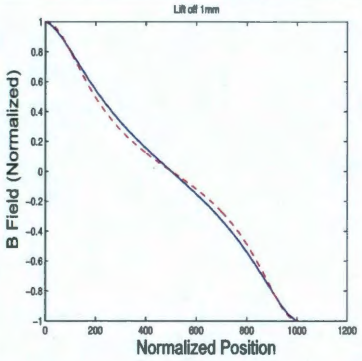	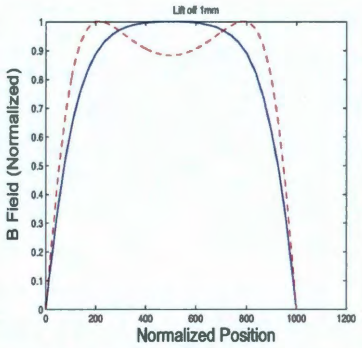	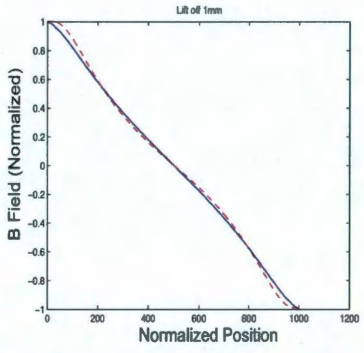	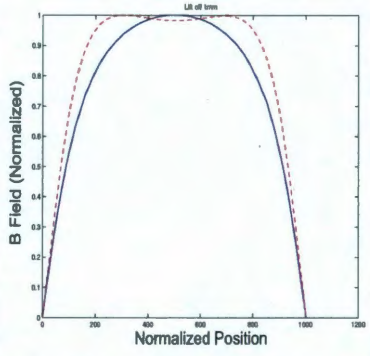
Trapezoid Defect 2		**Notch Defect**	
Radial Signal	Axial Signal	Radial Signal	Axial Signal
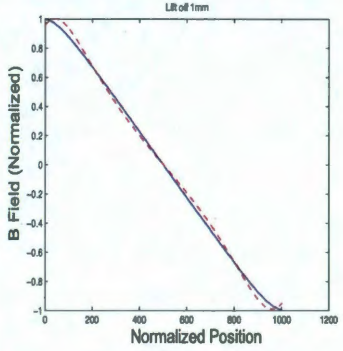	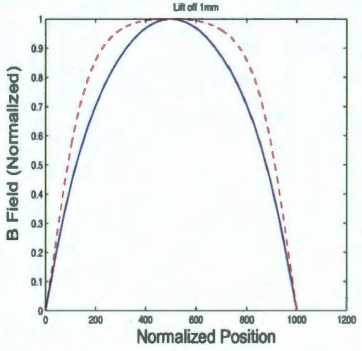	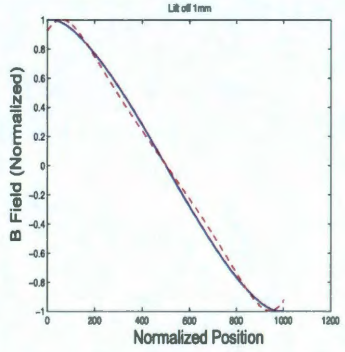	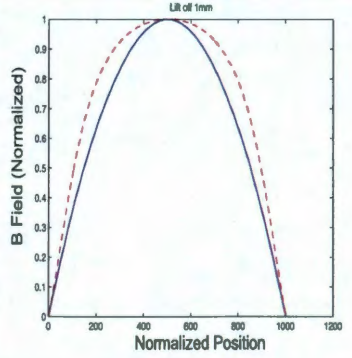

Referring to the previous table, it is possible to observe that the magnetic dipole model (red dashed line) and the FEM analysis (blue solid line) solutions did not match. Higher differences were shown at the axial signals and this occurred for different assumptions made for the MDM model. For instance, the higher differences were shown for the rectangular signal. Furthermore, it was discussed in Chapter Two how the defect's shape should approximate to an ellipsoidal cavity in order to successfully apply the MDM. A wide rectangular defect's shape does not approximates an ellipsoidal. As a result, a variable magnetic field inside the defect's cavity was present in these MFL's signal analysis performed by MDM which considered a constant magnetization term. Thus, the FEM model outcome should be more accurate for a non-ellipsoidal defect shape. Another possible reason for why different solutions can be expected between both models is because it was assumed at the MDM model's derivation that the relative magnetic permeability of the ferromagnet will be constant, which eliminate the contribution from the element's volumes (Equation 2.9). There also exists a direct connection between the relative magnetic permeability and the magnetization values of the defect elements which was presented in Chapter Two by (Equation 2.15). In contrast, the FEM model outcome depends of the B-H curve of the ferromagnet, which could be variable. In fact, the FEM model analysis did present variations of the relative magnetic permeability at the defect's walls. The following figure will show how the relative magnetic permeability of the defect elements will be a variable of the proposed defect's dimensions.

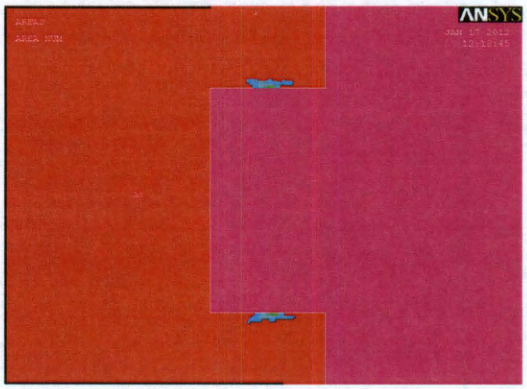

Figure 3.5: Variable Magnetic Permeability

The previous conclusions did not mean that MDM can not evaluate the proposed defect shapes. Earlier results of (Table 3.3) showed how the difference between the solutions of both models for the rectangular defect was high. It also showed how as the angles of the defect's walls were decreased, the difference between the models' solutions tended to reduced. This occurred because as the angels of the defect's walls keeps decreasing, the defect's shapes will tend to approximate more and more to an ellipsoidal shape. It was showed by Dutta showed that a narrow rectangular defect shape can be considered as an ellipsoidal shape. The following figure presents an analysis of a rectangular defect with the dimensions presented at the following defect shape.

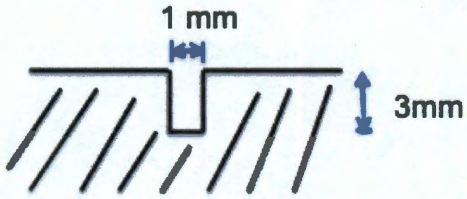

Figure 3.6: Rectangular Defect. Dimensions Modification

The next figure will present the axial MFL signal solutions performed by the two models. Both models obtained the same solution. From the following analysis it is possible to conclude that despite whether the values of magnetization of the elements of the defect are

constant or variable, the identification of the elements, the interpretation of the element's charge and the behavior of the elements will not change.

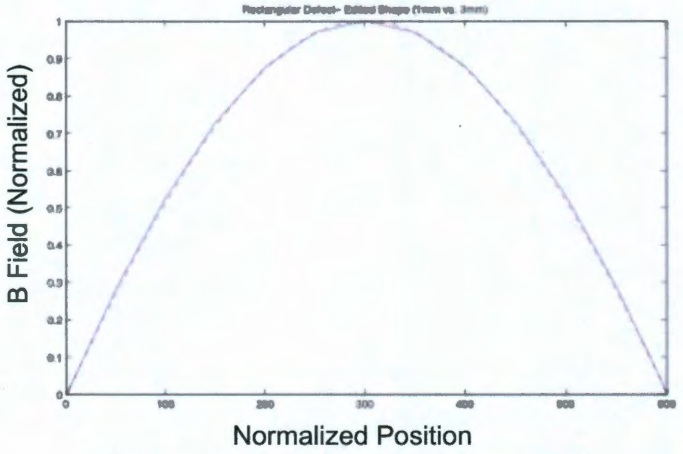

Figure 3.7: MFL's Signals Matched

The following section of this chapter will introduce an analysis of MFL signal readings. With reference to the proposed defect shapes, it has been addressed how the readings of MFL signals will receive contributions from a defect's walls for the proposed defect's dimensions. It will now be explained how the contribution from both defect wall elements reduce the definition of the characteristics of the closest wall's signal.

3.4 MFL Signal's Resolution

This section will present an analysis of how the contribution from further elements of the defect will bury the true characteristics of the defect's topology. For the analysis that this section will present, the defect dimensions will be varied. This section will present the MFL signals for the same analyzed wall's angles but with a variable center length (where the maximum depth is constant), and those lengths will be increased in order to observe the characteristics of the defect's signals, which will give a higher degree of information about the defect's topology. The following tables will present the different analysis performed as well as the dimensions that were used for each defect shape.

Table 3.4: Rectangular MFL Signals Variation- Defects Length Variation

	Radial Signal	Axial Signal
10 mm Length	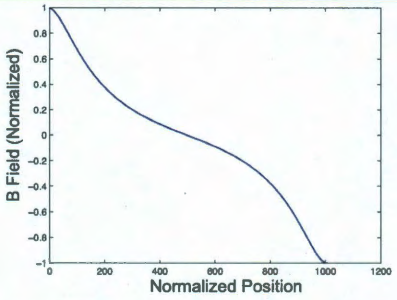	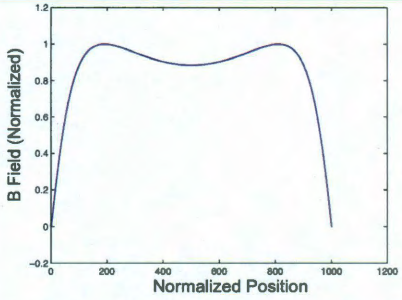
20 mm Length	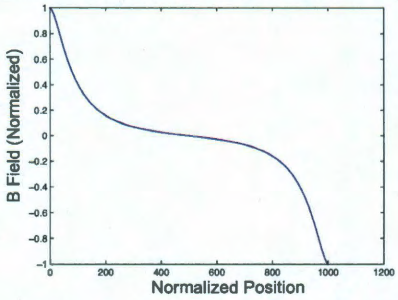	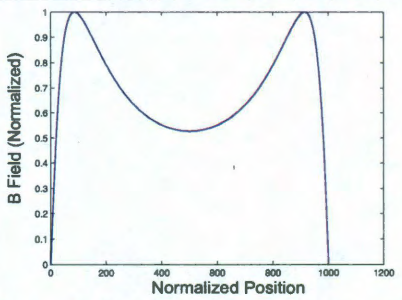
40 mm Length	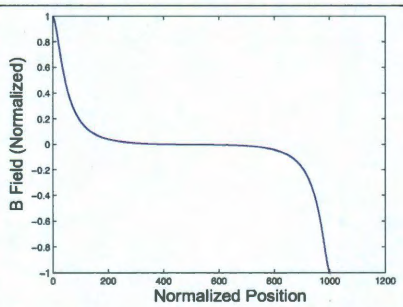	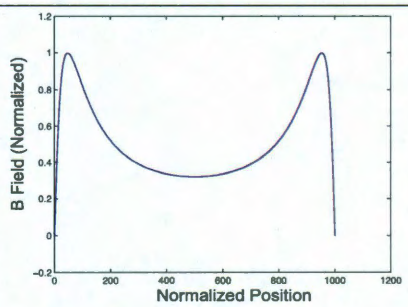
60 mm Length	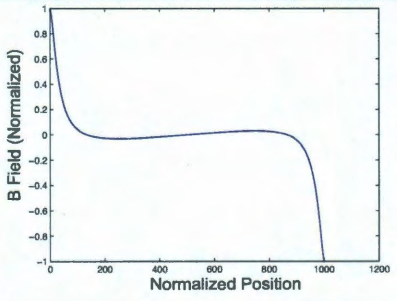	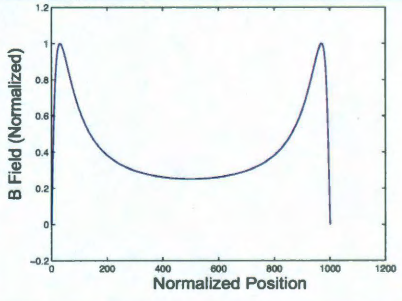

It is possible to observe how as the central length of the defect gets higher, the elements of one wall of the defect (elements that will contribute to the MFL's signals), will get farther from the other wall's elements and from its range of contribution. As a result, a more definite MFL signals can be observed, where the characteristics of the signal of one wall of the defect are not affected by the elements of the other defect's wall. It is also important to mention that as higher the central length of the defect is, higher variation of the magnetic permeability will exist among the defect's elements. There are a few observations that can be made from the signals obtained by this analysis.

With reference to the radial MFL signals, it is possible to observe how the rectangular defects elements tended to only affect the points that are near the defects edges. In the same way but analyzing the axial MFL signal, as the length between both defect's walls is increased, the element's contribution range (sensor's points which elements of the defect would reach) can also be observed. From the previous table it is possible to conclude that the range at which the elements of one wall will start to conflict with the range of contribution from the elements from the other defect's wall will be when the central length of the defect become smaller than $40mm$ for the radial signal and smaller than $60mm$ for the axial signal. The phenomenon occurs because the magnitude of contribution from the defect's elements will be much higher in an axial sense than in the radial sense as discussed earlier in this chapter. Of course, all the mentioned observations can be made with respect to a $1mm$ lift-off and a maximum defect's depth as was mentioned before. However, a similar analysis can be made for different defect parameters. The following table will present a the analysis of the other 3 defects using a $60mm$ length but with variations at the defect's walls angles . The angle at both defect's walls will be the ones used for trapezoid number one, trapezoid number two and the notch defect.

Table 3.5: Defects' MFL Signals Variation- 60mm Defects' Length

60mm Defects' Length	Radial Signal	Axial Signal
Trapezoid 1 Angle	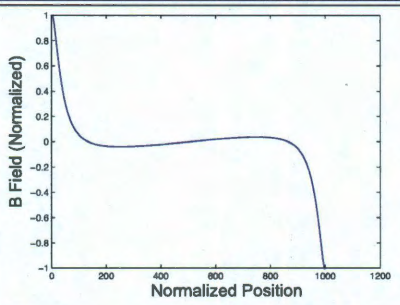	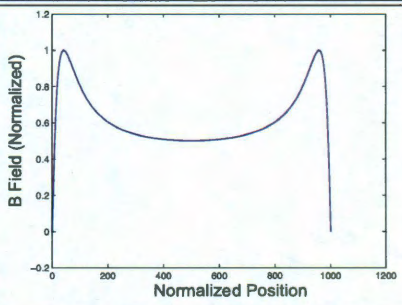
Trapezoid 2 Angle	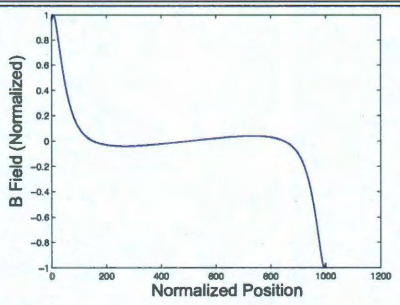	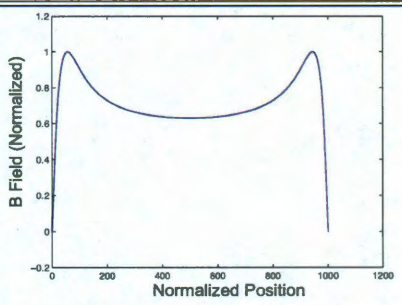
Notch Angle	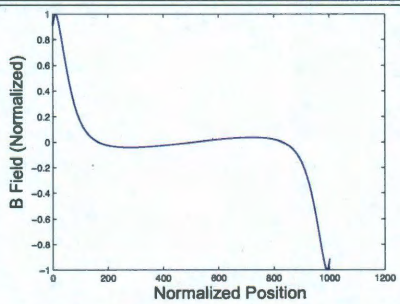	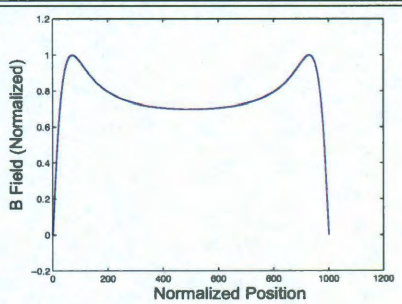

It is also possible to observe how as the angles of the defect wall decrease, the range of contribution from the defect's elements will reach points that the previous defect shape did not reach. Also, the range of influence of the elements of the wall can give a hint about the locations of the defect's bottom elements. It is possible to observe a wider section close by the edges of the radial's MFL signal as the wall's angle keeps decreasing. With reference to the axial signals, it is possible to observe the magnitude of the signal in within

the defect range get higher with respect to the maximum magnitude point of each signal as the angles of the walls decrease. Similarly to proceed with this parameterization study, the following tables will present the same analysis presented before but with the variation of $1mm$ for the depth of the defects (the maximum depth of the defect is of 2 mm). All three defects with variations at their walls preserved the same angle as before. The angle β will be as the initial defects presented them.

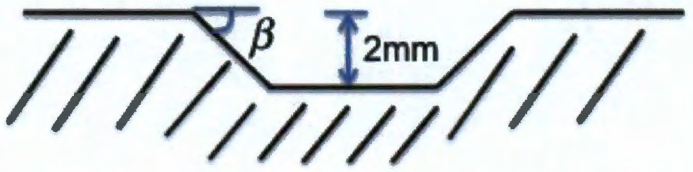

Figure 3.8: Parameterization Study

From the following analyses the conclusion can be drawn that when the central length of the defect is grater, the region of conflict for the signal's contribution of the defect's walls tended to vanished. Also it is possible to note at the radial signal ($60mm$), how the no constant magnetic permeability changes the defects' signals (it is possible to observe negative values for the radial signal in the positive polarity of the defect shape, as well as positive values at the negative polarity of the defect shape).

Table 3.6: Rec. MFL Signals Variation- Defects Length Variation ($2mm$ Max.t Depth)

	Radial Signal	Axial Signal
10 mm Length	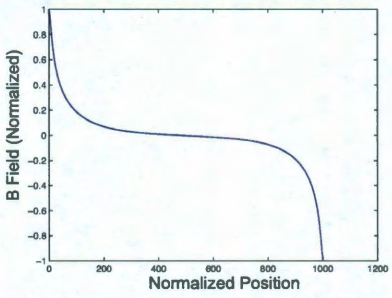	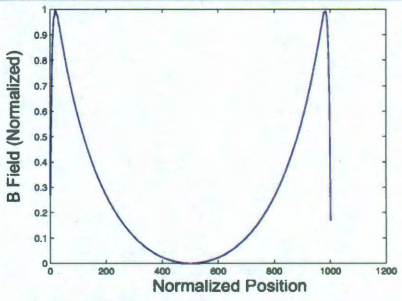
20 mm Length	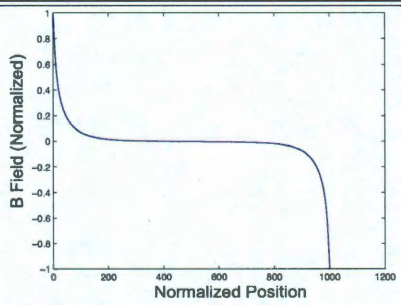	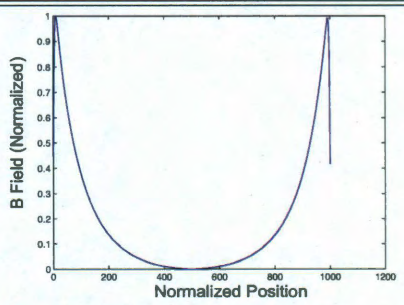
40 mm Length	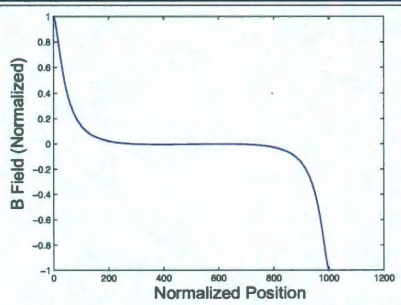	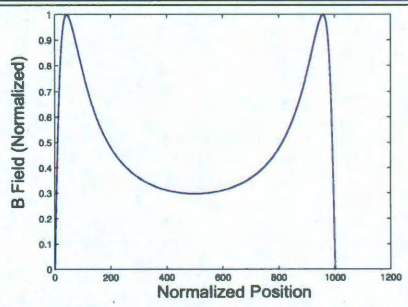
60 mm Length	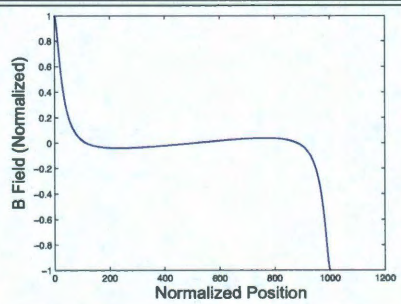	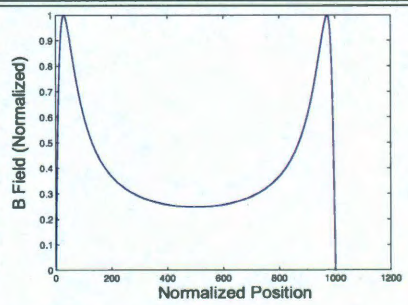

Table 3.7: Trapezoide 1 MFL Signals Variation- Defects Length Variation (*2mm* Max.t Depth)

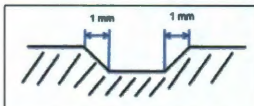	Radial Signal	Axial Signal
10 mm Length	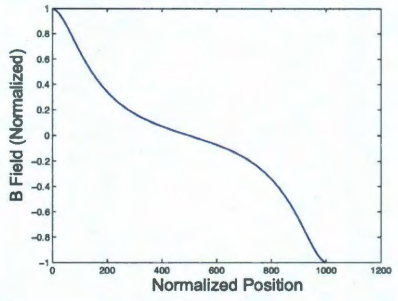	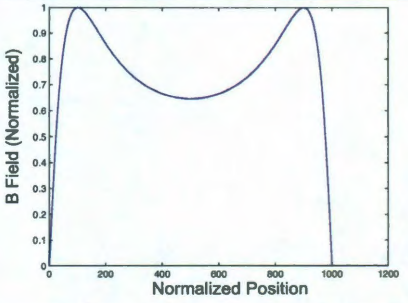
20 mm Length	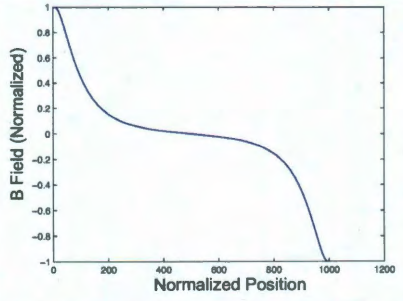	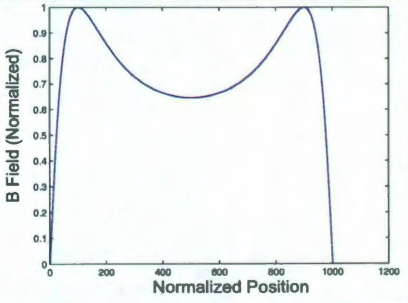
40 mm Length	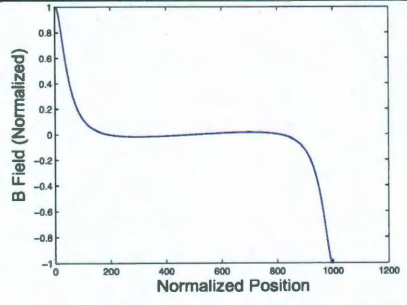	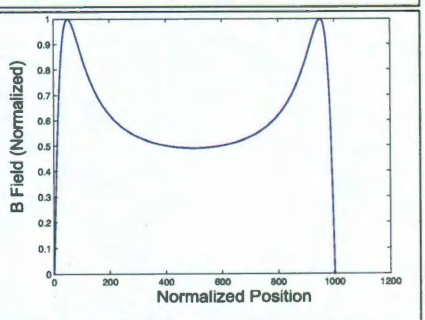
60 mm Length	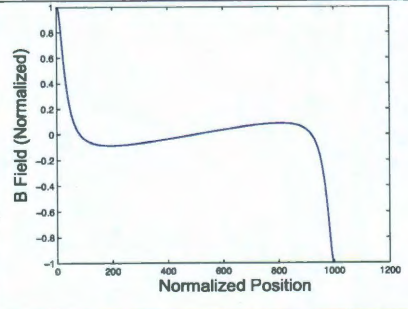	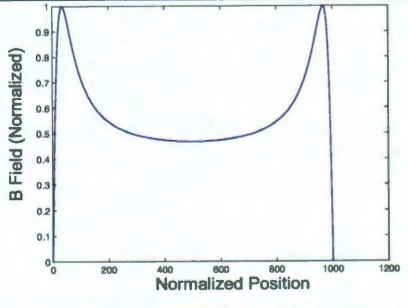

Table 3.8: Trapezoide 2 MFL Signals Variation- Defects Length Variation (2*mm* Max.t Depth)

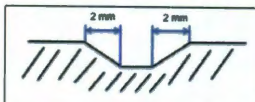	Radial Signal	Axial Signal
10 mm Length	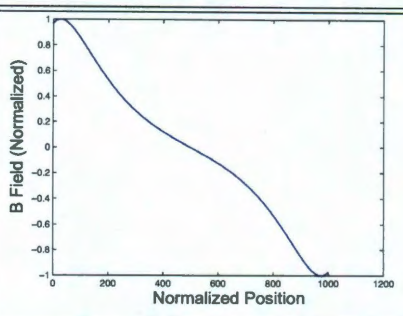	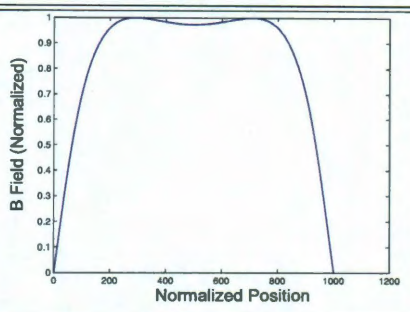
20 mm Length	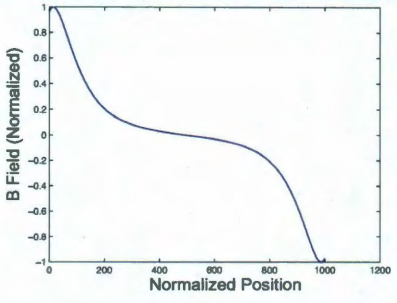	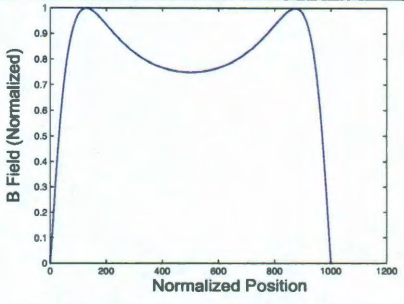
40 mm Length	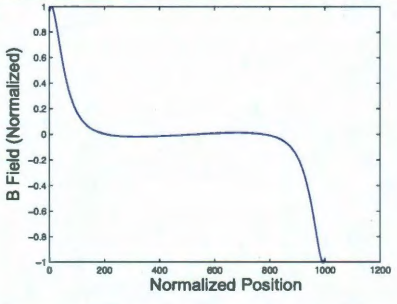	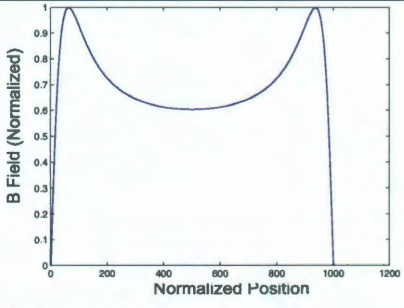
60 mm Length	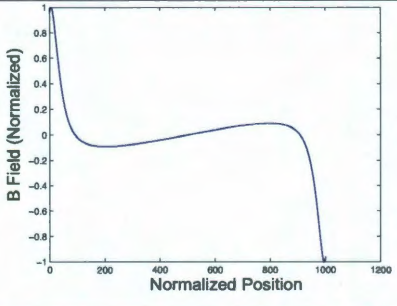	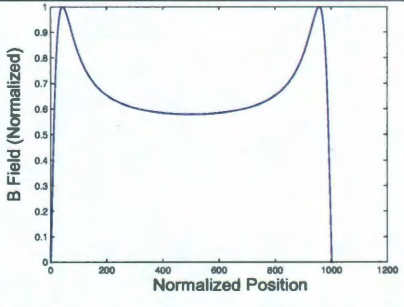

Table 3.9: Notch MFL Signals Variation- Defects Length Variation ($2mm$ Max.t Depth)

	Radial Signal	Axial Signal
10 mm Length	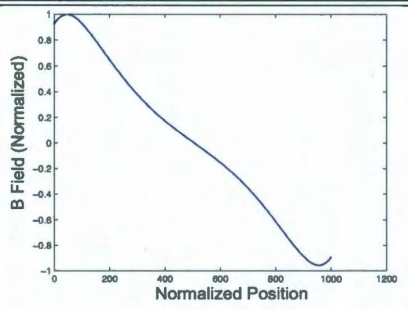	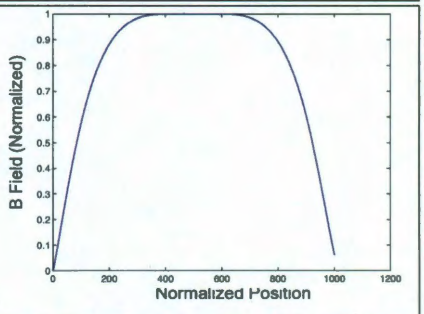
20 mm Length	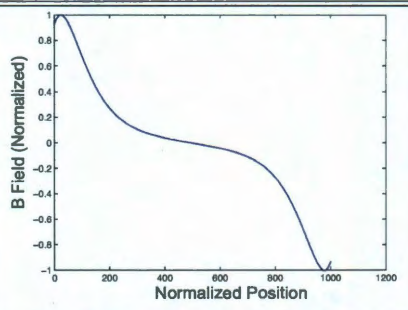	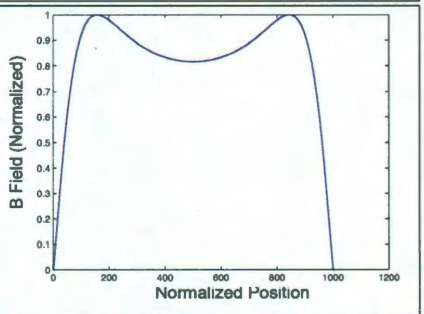
40 mm Length	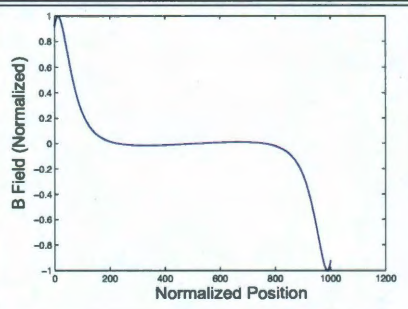	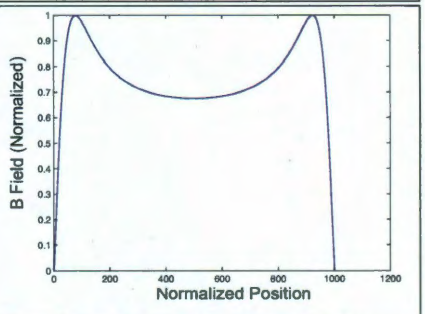
60 mm Length	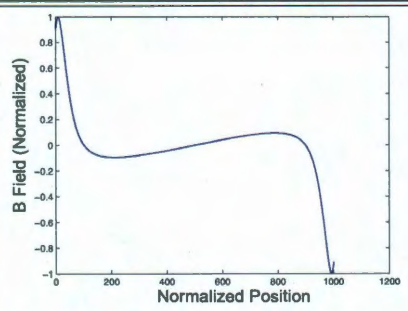	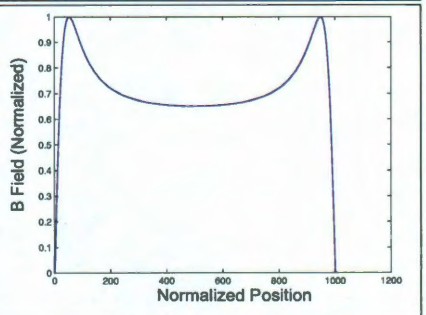

These analyses that were briefly discussed in this section presented how the topology characteristics of the MFL signals were affected by the same defect's topology and this happened as the dimension of the defect shapes got smaller. Furthermore, the elements of the same defect will change the MFL signal behavior. The complexity of the MFL inverse problem will become more difficult as the defect dimensions becomes smaller, although constant magnetic permeability tends to be present at smaller defects. The conclusion can be drawn that as further the defects' walls are, the amount of information reflected on the MFL signals regarding the defect's shape is greater but the magnetic permeability becomes variable.

The following chapter will introduce a wavelet analysis that only uses the MFL radial signals (for the original four defects section in 3.3), produced by the FEM models presented in the present chapter. Thus, the previous differences presented by the FEM model and the MDM will not be reflected in the following analysis. In summary, this chapter has presented a FEM model which was used to analyzed the same four different defects presented previously. Furthermore, the extracted results of the FEM model were compared to the results presented by the MDM and the main difference between both model's results were at in the MFL axial signal. It was posited that the magnetization of the defect's elements will be variable and the computations performed by the MDM should consider this variability parameter. The analysis that will be addressed in the following chapter only uses the radial's MFL signals extracted from the FEM simulations which computed more accurate MFL values.

Chapter 4

Wavelet Analysis

Many different techniques have been used in the MFL signal processing field, but none of them reach the main objective, which is the correct interpretation of the signal in order to have more information about the ferromagnet defect. Wavelet Analysis (WA) is without doubt one of the most powerful techniques that could be used for signal interpretation. Wavelet Analysis' development was a popular topic in the latest 80s. Researchers explored almost every aspect of the subject. Most of wavelet analysis theory is already written. However, wavelet analysis applicability could be considered as the actual exploration field; academics did impressive work describing the theory of this technique, but the applications field of this technique is still unexplored. Furthermore, in the MFL field it is commonly believed that wavelet analysis can only be used as a compression technique, due to the enormous amount of work in which wavelets techniques have been only used as a compression step of data storage procedure.

However, the preliminary work of wavelet analysis for interpretation of MFL signals has contributed to techniques to differentiate MFL signals for defect shapes with similar characteristics. Furthermore, one of the main advantages of wavelet analysis is that in the wavelet domain, signal separation is possible, while with techniques done in the time domain or frequency domain it is not possible to perform a signal separation. Hence, this advantage is a very important asset of wavelet analysis studies, since a closer characterizations of the signal can be studied, making possible a fuller and more clear understanding of the signal information.

4.1 Introduction

In this section a brief introduction of wavelet analysis technique will be addressed in which the basics points and descriptions will be explained. Given a signal of finite energy, this will be projected on a continuous and finite frequency bands. Furthermore, wavelet analysis procedure begins with a basic wavelet function commonly known as a mother wavelet. By shifting the mother wavelet function over the signal, a family of expansion functions can be generated. There exist many mother functions that can be used for a wavelet analysis, including:

- Gaussian
- Mexican hat
- Morlet
- Haar
- Daubechies
- Meyers

Each mother wavelet function has its own properties and characteristics. The analysis that presented in this thesis was done by applying Haar wavelet function. It should be noted that for wavelet analysis, the orthogonality of the system produced is of extreme importance. Although the orthogonality of the functions will be a sufficient condition for WA, this does not means that it is a necessary condition. Consequently, Haar wavelets produce the simple orthogonal wavelets system, due to scaling functions that this mother wavelet includes. The Haar wavelet function will be presented below.

$$\psi(t) = \begin{cases} 1 & 0 \leq \mathrm{t} < \frac{1}{2} \\ -1 & \frac{1}{2} \leq \mathrm{t} < 1 \\ 0 & \text{otherwise} \end{cases}$$

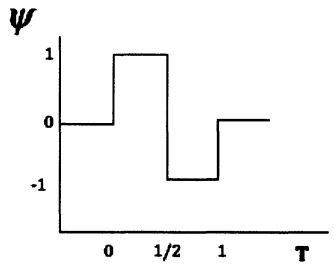

Figure 4.1: Haar Mother Wavelet Function

Further references to this topic were addressed by Burrus [1] and Oppenheim[20]. The Haar scaling functions also depend on time and usually are represented as ϕ(t). The following figure presents the time effective interval of the function.

$$\phi(t) = \begin{cases} 1 & 0 \leq t < 1 \\ 0 & \text{otherwise} \end{cases}$$

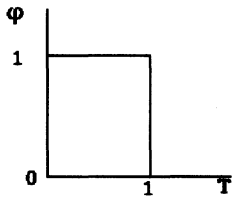

Figure 4.2: Haar's Scaling Function

With the wavelet and scaling function that were used for the analysis defined, it will be possible to introduce any given signal and represent it by the two elements described before. Let's call a real MFL signal f_i, which index "i" will take the form of "r" for the radial MFL signal component and "a" for the axial MFL signal component. The following equation presented by Burrus[1] will represent a signal constructed by $c_{k,j=N}$ and $d_{k,j}$ which are the signal's approximation and detail coefficients multiplied by the scaling function as well as the wavelet function respectively:

$$f_i(t) = \sum_{k=-\infty}^{\infty} C_{j=N} 2^{j/2} \phi(2^j t - k) + \sum_{j=0}^{N} \sum_{k=-\infty}^{\infty} d_{k,j} 2^{j/2} \psi_k(2^j t - k), \tag{4.1}$$

where N represents the maximum decomposition level. The WA consists in computing the signal's coefficients and then the computation of the multiplication of those coefficients with the respective function (scaling or wavelet). The following section will address the MFL signal's wavelet analysis.

4.2 Preliminary Work of Wavelet Analysis For MFL Signals Characterization

This section addresses how wavelet analysis was used to analyze MFL signals. The MFL extracted signals from the FEM model were used for the matter of wavelet analysis. The FEM model as was addressed in the previous chapter has two major advantages for theoretical research. First, FEM analysis will not add any noise to the MFL signals, and second, the defect's shape can be strictly controlled. Once the signals were normalized for comparison purposes, the Matlab wavelet toolbox could be used to performed the multi resolution wavelet analysis of each signal component individually. This section will present the results of the performed wavelet analysis, which used the MFL's radial signals of different defect shapes. Recall the results shown in tables (3.1) and (3.2). The first table contains the display solution of the FEM analysis of the four defects in which the areas of higher MFL signal magnitude were highlighted. The second table presents the extracted radial signals that were used for this wavelet analysis. However, both models' signals can be used for this analysis. Since the FEM's extracted signals were more accurate, those signals were used.

The first analyzed defect that will be presented is the rectangular geometry study. The radial FEM solution of the rectangular defect signal that has been presented in table (3.1) showed a higher magnitude of MFL which occurred near the edges of the defect. Likewise, the following table will present the radial signal of the four different defect shapes. The difference between these radial signals and those ones presented in table (3.2) is that

each plot will present a bigger signal length than the 6 mm standard defect chosen as an example for this work. In other words, the dimensions of the defect are fixed but the length that was considered for the plot was of $10mm$, $5mm$ before and after the center of the defect (the plots will include points outside the defect range). It is important to mention that the signals that will be analyzed were extracted from the FEM analysis because as was discussed in Chapter Three, the big difference that were observed and pointed out in Chapter Two between the different defect's signals can no longer be observed in FEM signals because of the variable magnetization value. Consequently, analyzing the following MFL signals that turned out to be very similar to each other will result in a more difficult and challenging procedure.

Table 4.1: 4 Defects - Finite Element Analysis MFL Radial Signal.

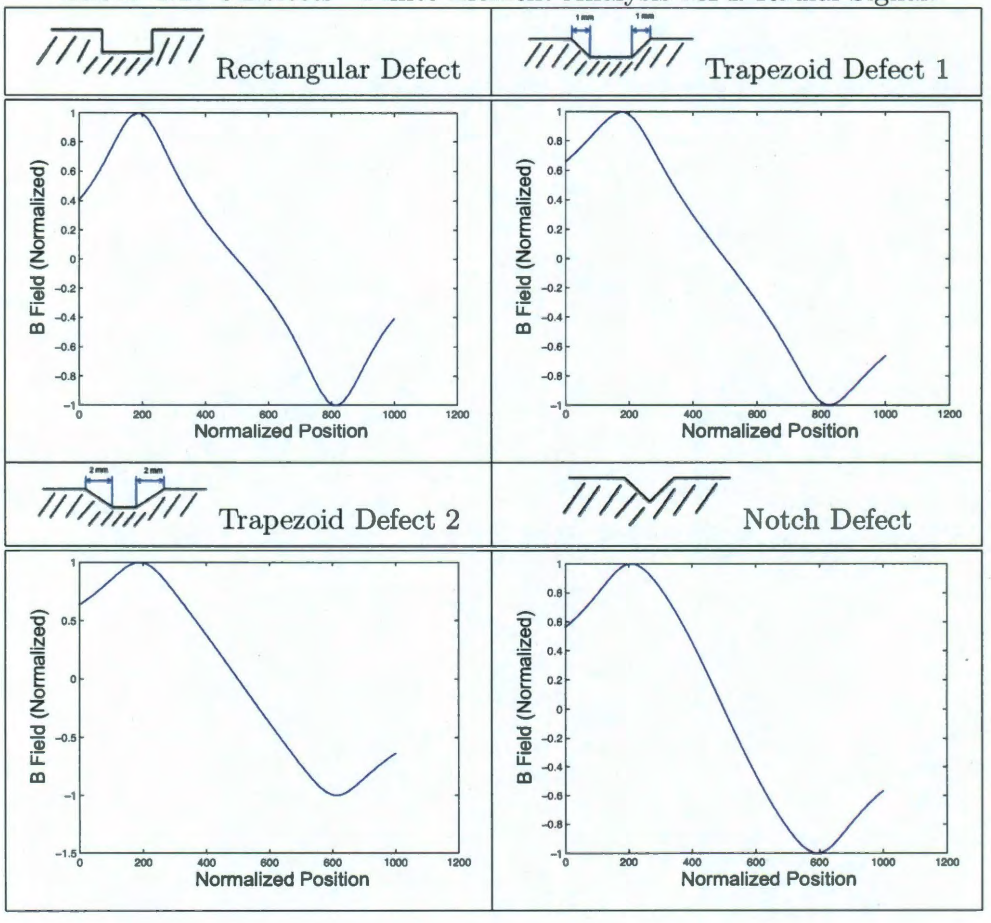

It is possible to observe that both trapezoid's signals as well as the notch defect signal turned out to be very similar among them (almost a straight line between maximum and minimum point). These similarities will result in a more difficult task for MFL inspectors wanting to interpret the signals. Similarly, the distinctions made in those same signals but which were modeled by the MDM are not as evident for signals modeled by FEM. Consequently, the interpretation of the MFL signals will be very difficult without any additional aid. Therefore, figure (4.3) presents the multilevel wavelet analysis performed for the rectangular radial signal. The signal, which is composed of 1000 points, was analyzed and the WA procedure reached the eighth resolution level. The following figure is composed of 10 plots (Space Position vs. Scaled Tesla Magnitude) with descriptions are as follow:

1. The first plot (top to bottom), is the original signal.
2. The second plot represents the analysis of the approximate coefficients of the highest decomposition signal level.(In this case, eight level)
3. The third plot represents the analysis of the detail coefficients of the highest decomposition signal level.
4. The following plots (fourth to tenth) represent the detail coefficient analysis of each decomposition level order from higher level to lower level (The first level will be at the bottom of the figure).

Recalling equation (4.1), the second plot represents the approximation function for the MFL signal which can be identified as the first summation of the equation. The following eight plots represent the detail functions of the eight different levels of resolution. The following equation presents equation (4.1) for the radial MFL signal. This equation is presented with a multicolor text, which will help to identify what each plot represents with reference to Figure(4.3),

$$f_r(t) = \sum_{k=-\infty}^{\infty} C_{j=N} 2^{j/2} \phi(2^j t - k) + \sum_{j=0}^{N} \sum_{k=-\infty}^{\infty} d_{k,j} 2^{j/2} \psi_k(2^j t - k), \tag{4.2}$$

where at each level of resolution j, there will be a detail function (green summation).

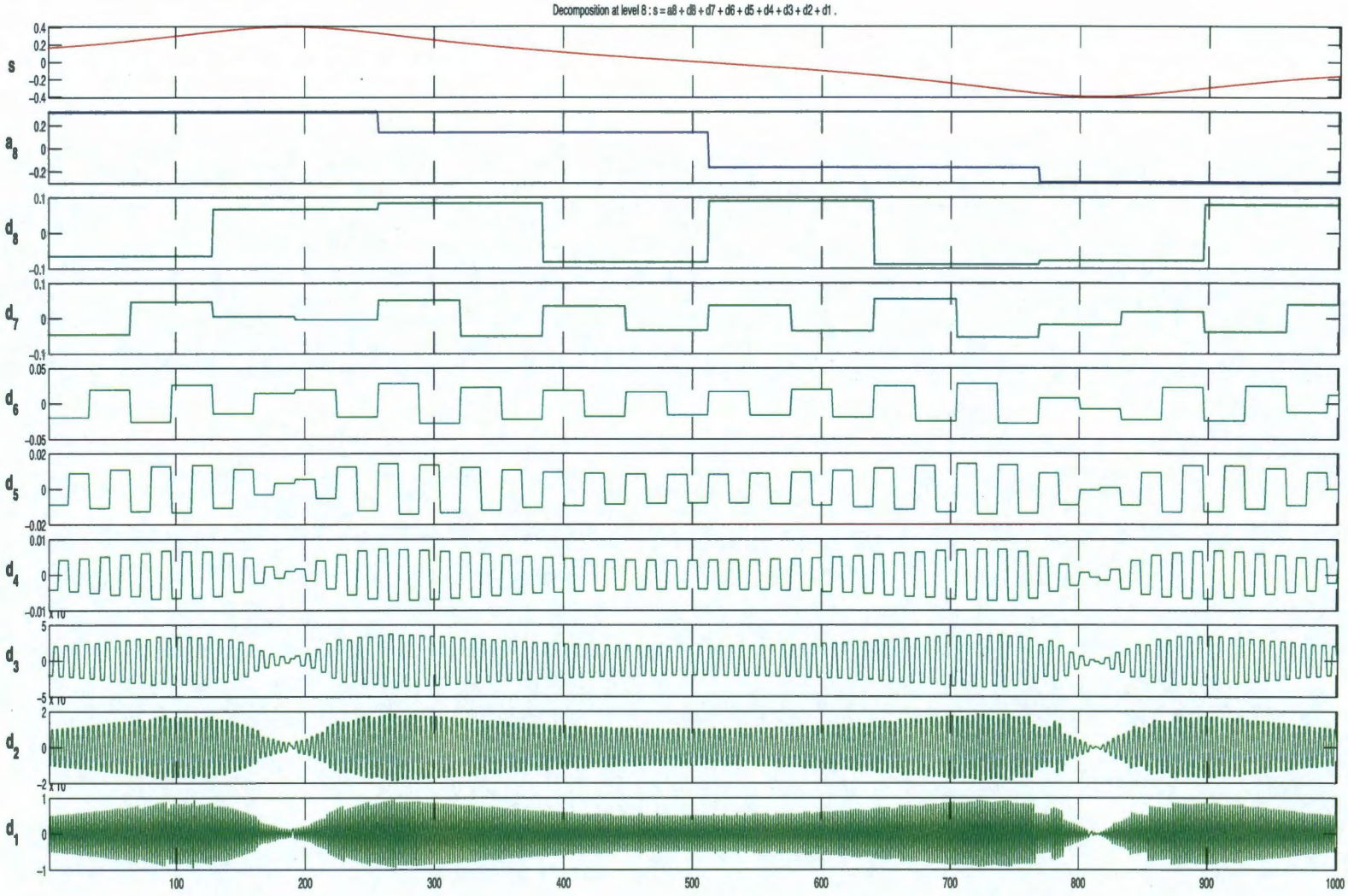

Figure 4.3: Muli Level Wavelet Analysis - Rectangular Defect

One of the most interesting signal behaviors was observed at the first level of resolution in the detail signal (bottom plot of Figure (4.3)). The following table presents the results of wavelet analysis that were performed for the MFL radial signals of the four different defects.

Table 4.2: Four Defects - Wavelet Analysis MFL Signals- First Resolution Level.

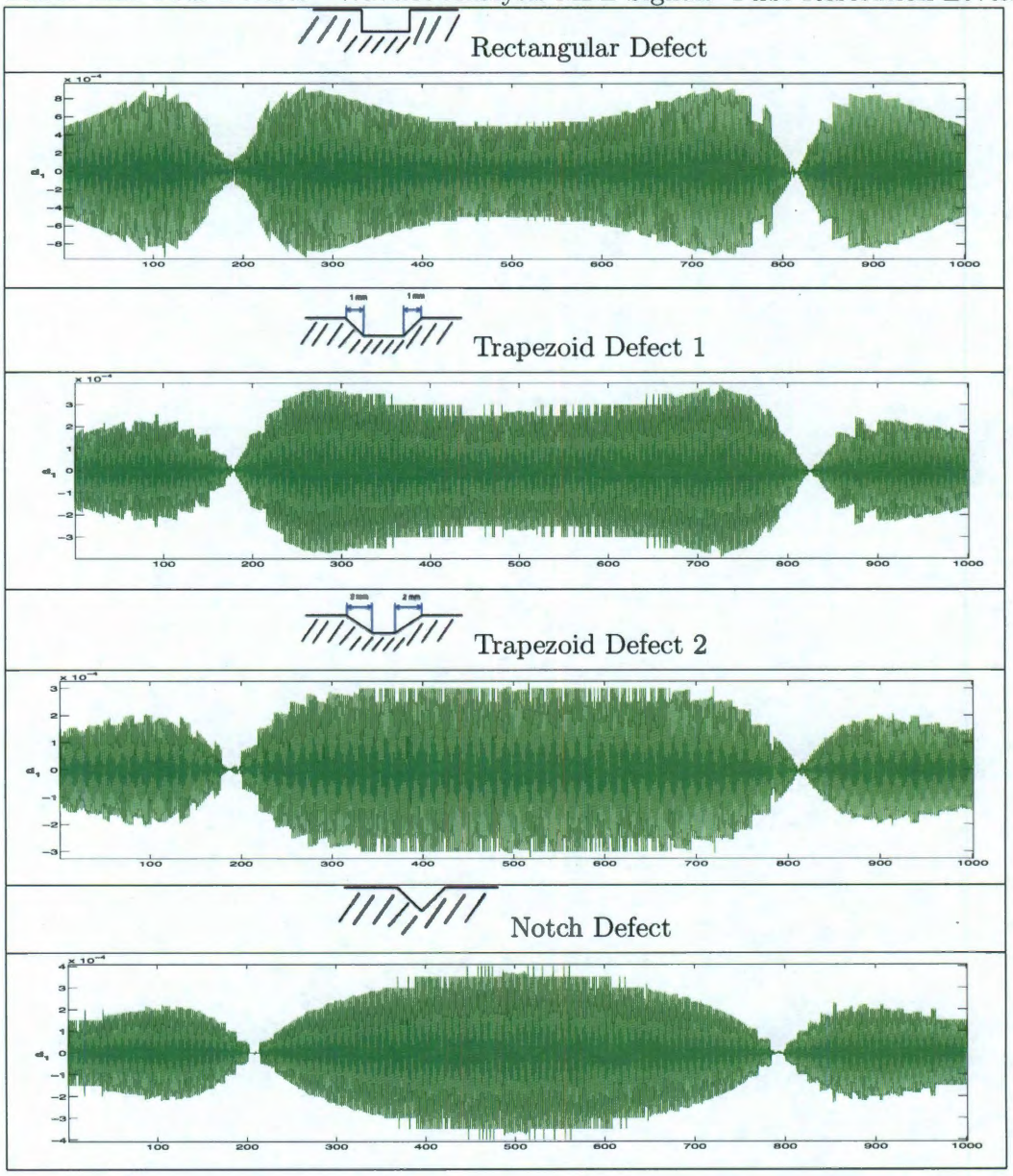

Despite all MFL signals being very similar. It is possible to observe that by using wavelet analysis, differences among the signals can be easily observed and quantified. In the same context it is possible to make the following observations about the plots that were presented in Table (4.2) :

1. The magnitude of the detail coefficient function will keep decreasing as the wall's angle keeps decreasing. This can be corroborated by using either the MDM or FEM models. Let us consider the rectangular defect for a moment. This defect shows high concentration of MFL, precisely at the defect's edge. When a defect has a wall with an angle, as do any of the other three proposed defects, the concentration of MFL tends to distribute along the defect's length. As a result, the magnitude of the signals will tend to reduce.

2. The magnitude of points closer to the defect's edge, which are located outside the defect's range, will decrease in a more accelerated way than the magnitude of points P located within defect's range. This can also be explained by analyzing the defect shapes with the MDM and FEM models. For instance, with reference to the following figure, if a rectangular defect is analyzed, it is possible to state that $P1$ and $P2$ will have the same magnitude.

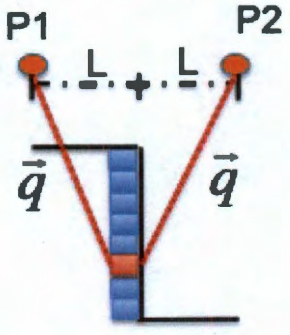

Figure 4.4: Contribution to Points P closer to the Edge-Rectangular Defect

But then a wall with a certain angle is introduced instead. As a result, $P2$ will

get higher contributions from the wall's elements with respect to $P1$. This occurs because $P2$ will be closer to all the wall's elements (Figure 4.5).

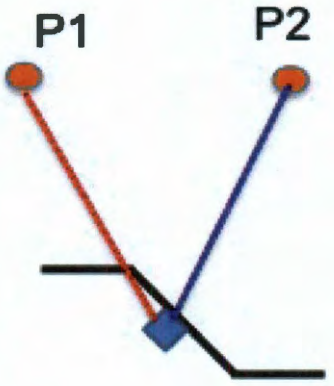

Figure 4.5: Contribution to Points P closer to the Edge- Variable Angle β

Similarly, the previous figure shows why the distances relation of an element changed when an angle in present at a wall. The conclusion can be drawn that the same element will give higher contribution to on length of the signal (P2 and points close to it) and will give less contribution to another portion of the signal's length (P1 and points close to it). This means that the elements tend to make less contribution to those points, which reduce the MFL concentration at the edges, giving a smaller MFL magnitude.

3. The behavior of the detail functions near the defect's center, also exposes the signal behavior in within the defect's range. These behaviors could not be observed by a simple eye inspection. Recalling the descriptions that were discussed in Chapter Tow, we can make the following comparisons between the WA of each signal and the descriptions in Chapter Two:

    - Rectangular Defect shape: It has been stated that a lack of contributions occurred over those points P which were closer to the defect's center. The description of the rectangular defect signal in that respect was addressed in Chapter

Two (with reference to Figure(2.9)). The lack of contribution was noted or characterized as concave curves close by the edges and then a straight line between those two curves. In the same way, by observing the WA results, it is possible to observe how greater differences occur near the edges and then a constant difference between neighboring points connects these two parts of the signal (first figure of Table (4.2)). It is important to point out that a straight line from an MFL signal can be interpreted as a constant ratio of magnitude reduction or increment.

- Trapezoid 1: This defect's signal showed in Chapter Two how the curves (lack of contributions in within defect's range) tended to vanish as the defect's elements got closer. The MFL signal extracted from the FEM model presented almost a straight line between the maximum and minimum points, and despite these apparent characteristics of the MFL signal analyzed by a naked eye inspection, the WA outcome showed how those curves were also presented in the FEM signal. (Reference Figure(2.15) and the second plot of Table (4.2)).

- Trapezoid 2: Likewise, recalling the analysis of Figure (2.19) , it was possible to observe two small curves near the edges within the defect's range and a straight line that connected the two curves. Again, the FEM's extracted signal did not present those curves, but the WA results clearly showed an increase of difference between neighboring points (from point 200 to 340) and then a constant difference between neighboring points (a similar behavior a the other end of the WA analysis due the symmetry of the defect). These two behaviors also matched.

- Notch: The analyzed signal proposed by the MDM showed almost a straight line between both points (maximum and minimum points). However the WA suggested a very small and smooth curve near each edge and then a linear relation between neighboring points.

In summary it is possible to state that WA of the MFL signals will decompose the signal details with the objective of disclosing every incident of the MFL signal in order to observe the small details and behaviors that cannot be observed with at simple eye inspection. This chapter will conclude by presenting the following table which contains a comparison between the different analyzed defect shapes, the MFL's signal extracted from the FEM model, and the expected WA signal shape.

Table 4.3: Wavelet Analysis MFL Signals- Defect's Characterization

Defect Shape	Radial MFL Signal	Wavelet Components of MFL Signal
	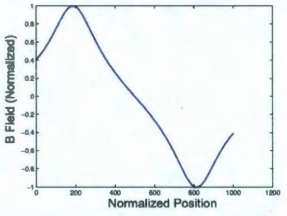	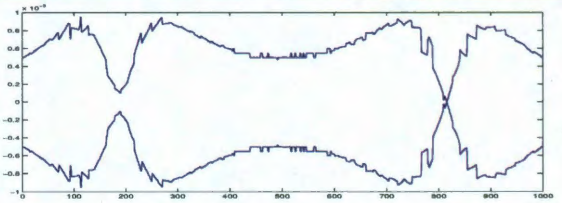
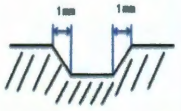	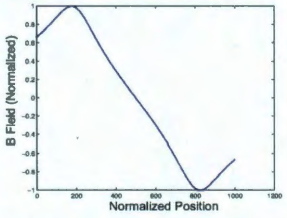	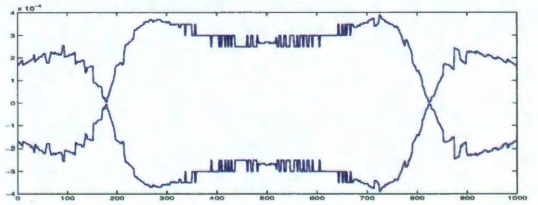
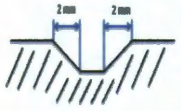	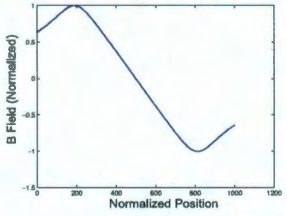	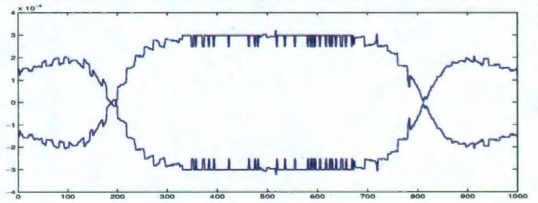
	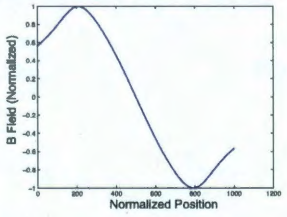	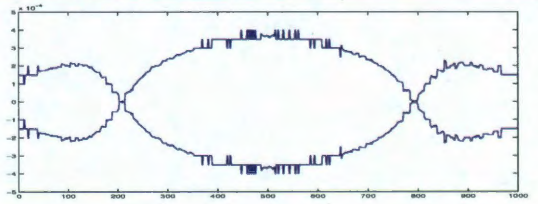

The ultimate objective of this research investigation is to solve the inverse problem. The previous described technique could help to describe at some level the defect geometry. Without doubt the preliminary work presented in this chapter as well as the analysis of the forward problem presented in Chapters Two and Three would be the first and fundamental step to solve the inverse problem in which from MFL signal analysis it could be possible to discover a defect's shape. The following chapter presents the conclusion of this thesis in which a summary of the results will be addressed, as well as the importance of the results and possible further projects.

Chapter 5

Conclusions

MFL methodology as well as other pipe inspection techniques have been used in the last decades as a defect detection tool, ignoring all the extra collected information that each technique has obtained from the analyzed structure. This luxury is no longer acceptable for most different industries. The analysis of the collected signals could give a great deal of information about the type of failure in the structure. Thus, the evaluation of the level of threat that an identified defect represents to a given structure is fundamental in this field. The fundamental concepts that were introduced in this work could give a great deal of importance to the interpretation of the MFL signals.

This work has presented a fundamental knowledge of how the MFL technique can be applied to ferromagnetic materials and how MFL signals are formed. This thesis also introduced a new methodology to analyze the MFL signals, allowing a more detailed inspection of the MFL signal. The adopted methodology showed how wavelet analysis could give a great deal of extra information about the analyzed defect shape. Therefore, the first contribution of this work is to provide insight into the dynamics of MFL in defects and how the MFL signals are computed. The second contribution of this thesis is to give a new path for MFL signal analysis which will lead to a better interpretation of the signals. This will lead to improving the accuracy and reliability of MFL technique.

The fundamentals addressed by this work open new research perspectives in this field. In fact, several related issues need to be analyzed. For instance, by applying the described dynamics of the MFL signals in conjunction with the introduced wavelet analysis, methodology which gives more information about the ferromagnetic defects shape should be proposed. Once this methodology has been proposed, the major drawback of pipe inspection techniques will be eliminated.

Appendix A

Rectangular Defect FEM Code - Different Lift-Off

This code was designed for ANSYS V12 platform. This program will measure MFL density at different Lift−offs.

```
    /prep7
ET,1,Plane53
Keyopt,1,1,0
Keyopt,1,2,0
Keyopt,1,3,1
Keyopt,1,4,0
Keyopt,1,5,0
Keyopt,1,7,0

MP,murx,1,1
TB,BH,2,,24,,

TBPT,,2806,0.4203
TBPT,,5133,0.9254
TBPT,,7538,1.3454
TBPT,,9847,1.5953
TBPT,,12136,1.7246
TBPT,,14444,1.8016
TBPT,,16772,1.8589
TBPT,,19093,1.9053
TBPT,,21423,1.9443
TBPT,,23755,1.979
TBPT,,26087,2.01
TBPT,,28411,2.0377
TBPT,,30743,2.0624
TBPT,,33074,2.0848
TBPT,,35410,2.1047
TBPT,,37736,2.1224
TBPT,,40068,2.1385
TBPT,,42401,2.1531
TBPT,,44731,2.1656
TBPT,,49394,2.1902
TBPT,,51719,2.2014
TBPT,,54052,2.2124
TBPT,,56390,2.2229
TBPT,,58716,2.2325

K,1,0,-2,0
K,2,0,2,0
K,3,.2,2,0
K,4,.2,-2,0
K,5,.2,-1,0
K,6,.2,1,0
K,7,.21,2,0
K,8,.21,-2,0
K,9,.21,-1,0
K,14,.21,1,0
K,15,.39,-2,0
K,16,.39,2,0
K,17,.4,-2,0
K,18,.4,2,0
K,19,.4,-.05,0
K,20,.4,.05,0
K,21,.45,.05,0
K,22,.45,-.05,0
K,23,1.2,-2,0
```

```
K,24,1.2,2,0
K,25,.21,-.5,0
K,26,.21,-.5,0
K,27,.21,.5,0
K,28,.21,.5,0
K,31,.21,.003,0
K,33,.207,-.003,0
K,32,.207,.003,0
K,34,.21,-.003,0
K,41,.21,.006,0
K,42,.21,-.006,0

   A,1,2,3,6,5,4
A,4,5,9,8
A,5,6,14,41,31,32,33,34,42,9
A,6,3,7,14
A,8,9,42,34,33,32,31,41,14,7,18,20,19,17
A,19,20,21,22
A,17,19,22,21,20,18,24,23
nummrg,all
/pnum,area,1
/replot
aplot

   Mp,murx,4,1

ASEL,s,area,,1,1
AATT,1
ASEL,s,area,,2,2
AATT,1
ASEL,s,area,,3,3
AATT,2
ASEL,s,area,,4,4
AATT,1 ASEL,s,area,,5,5
AATT,1
ASEL,s,area,,6,6
AATT,4
ASEL,s,area,,7,7
AATT,1
ASEL,all

   ESIZE,0.02
LESIZE,4,,,5500,,,,,1
LESIZE,11,,,2750,,,,,1
LESIZE,12,,,50,,,,,1
LESIZE,13,,,50,,,,,1
LESIZE,14,,,50,,,,,1
LESIZE,15,,,50,,,,,1
LESIZE,16,,,50,,,,,1
LESIZE,17,,,2750,,,,,1

   LESIZE,22,,,40,,,,,1

   AMESH,all

   BFA,6,JS,,,100000000

   FINISH

   /solu
solve
FINISH

/post1
Path,med,2,,1000
ppath,1,,.2105,-.005
ppath,2,,.2105,.005
pdef,,b,sum,avg
pdef,,b,x,avg
pdef,,b,y,avg

Path,med5,2,,1000
ppath,1,,.2105,-.005
ppath,2,,.2105,.005
pdef,,b,sum,avg
pdef,,b,x,avg
```

```
pdef,,b,y,avg

Path,med4,2,,1000
ppath,1,,.2104,-.005
ppath,2,,.2104,.005
pdef,,b,sum,avg
pdef,,b,x,avg
pdef,,b,y,avg

Path,med3,2,,1000
ppath,1,,.2103,-.005
ppath,2,,.2103,.005
pdef,,b,sum,avg
pdef,,b,x,avg
pdef,,b,y,avg

Path,med2,2,,1000
ppath,1,,.2102,-.005
ppath,2,,.2102,.005
pdef,,b,sum,avg
pdef,,b,x,avg
pdef,,b,y,avg

Path,med1,2,,1000
ppath,1,,.2101,-.005
ppath,2,,.2101,.005
pdef,,b,sum,avg
pdef,,b,x,avg
pdef,,b,y,avg


    Path,med001,2,,1000
ppath,1,,.21001,-.005
ppath,2,,.21001,.005
pdef,,b,sum,avg
pdef,,b,x,avg
pdef,,b,y,avg
```

Appendix B

Trapezoid Defect FEM Code - Different Lift-Off

This code was designed for ANSYS V12 platform. This program will measure MFL density at different Lift−offs.

```
/prep7
ET,1,Plane53
Keyopt,1,1,0
Keyopt,1,2,0
Keyopt,1,3,1
Keyopt,1,4,0
Keyopt,1,5,0
Keyopt,1,7,0

MP,murx,1,1
TB,BH,2,,24,,

TBPT,,2806,0.4203
TBPT,,5133,0.9254
TBPT,,7538,1.3454
TBPT,,9847,1.5953
TBPT,,12136,1.7246
TBPT,,14444,1.8016
TBPT,,16772,1.8589
TBPT,,19093,1.9053
TBPT,,21423,1.9443
TBPT,,23755,1.979
TBPT,,26087,2.01
TBPT,,28411,2.0377
TBPT,,30743,2.0624
TBPT,,33074,2.0848
TBPT,,35410,2.1047
TBPT,,37736,2.1224
TBPT,,40068,2.1385
TBPT,,42401,2.1531
TBPT,,44731,2.1656
TBPT,,49394,2.1902
TBPT,,51719,2.2014
TBPT,,54052,2.2124
TBPT,,56390,2.2229
TBPT,,58716,2.2325

K,1,0,-2,0
K,2,0,2,0
K,3,.2,2,0
K,4,.2,-2,0
K,5,.2,-1,0
K,6,.2,1,0
K,7,.21,2,0
K,8,.21,-2,0
K,9,.21,-1,0
K,14,.21,1,0
K,15,.39,-2,0
K,16,.39,2,0
K,17,.4,-2,0
K,18,.4,2,0
K,19,.4,-.05,0
K,20,.4,.05,0
K,21,.45,.05,0
K,22,.45,-.05,0
K,23,1.2,-2,0
```

```
K,24,1.2,2,0
K,25,.21,-.5,0
K,26,.21,-.5,0
K,27,.21,.5,0
K,28,.21,.5,0
K,31,.21,.003,0
K,33,.207,-.001,0
K,32,.207,.001,0
K,34,.21,-.003,0
K,41,.21,.006,0
K,42,.21,-.006,0


   A,1,2,3,6,5,4
A,4,5,9,8
A,5,6,14,41,31,32,33,34,42,9
A,6,3,7,14
A,8,9,42,34,33,32,31,41,14,7,18,20,19,17
A,19,20,21,22
A,17,19,22,21,20,18,24,23
nummrg,all
/pnum,area,1
/replot
aplot


   Mp,murx,4,1

ASEL,s,area,,1,1
AATT,1
ASEL,s,area,,2,2
AATT,1
ASEL,s,area,,3,3
AATT,2
ASEL,s,area,,4,4
AATT,1
ASEL,s,area,,5,5
AATT,1
ASEL,s,area,,6,6
AATT,4
ASEL,s,area,,7,7
AATT,1
ASEL,all

   ESIZE,0.02
LESIZE,4,,,5500,,,,,1
LESIZE,11,,,2750,,,,,1
LESIZE,12,,,40,,,,,1
LESIZE,13,,,60,,,,,1
LESIZE,14,,,30,,,,,1
LESIZE,15,,,60,,,,,1
LESIZE,16,,,40,,,,,1
LESIZE,17,,,2750,,,,,1


   LESIZE,22,,,40,,,,,1

   AMESH,all

BFA,6,JS,,,8000000

   FINISH

   /solu
solve
FINISH

/post1
Path,med,2,,1000
ppath,1,,.2105,-.005
ppath,2,,.2105,.005
pdef,,b,sum,avg
pdef,,b,x,avg
pdef,,b,y,avg

Path,med5,2,,1000
ppath,1,,.2105,-.005
ppath,2,,.2105,.005
pdef,,b,sum,avg
pdef,,b,x,avg
```

```
pdef,,b,y,avg

Path,med4,2,,1000
ppath,1,,.2104,-.005
ppath,2,,.2104,.005
pdef,,b,sum,avg
pdef,,b,x,avg
pdef,,b,y,avg

Path,med3,2,,1000
ppath,1,,.2103,-.005
ppath,2,,.2103,.005
pdef,,b,sum,avg
pdef,,b,x,avg
pdef,,b,y,avg

Path,med2,2,,1000
ppath,1,,.2102,-.005
ppath,2,,.2102,.005
pdef,,b,sum,avg
pdef,,b,x,avg
pdef,,b,y,avg

Path,med1,2,,1000
ppath,1,,.2101,-.005
ppath,2,,.2101,.005
pdef,,b,sum,avg
pdef,,b,x,avg
pdef,,b,y,avg


    Path,med001,2,,1000
ppath,1,,.21001,-.005
ppath,2,,.21001,.005
pdef,,b,sum,avg
pdef,,b,x,avg
pdef,,b,y,avg
```

Appendix C

Notch Defect FEM Code - Different Lift-Off

This code was designed for ANSYS V12 platform. This program will measure MFL density at different Lift−offs.

```
   /prep7
ET,1,Plane53
Keyopt,1,1,0
Keyopt,1,2,0
Keyopt,1,3,1
Keyopt,1,4,0
Keyopt,1,5,0
Keyopt,1,7,0

MP,murx,1,1
TB,BH,2,,24,,

TBPT,,2806,0.4203
TBPT,,5133,0.9254
TBPT,,7538,1.3454
TBPT,,9847,1.5953
TBPT,,12136,1.7246
TBPT,,14444,1.8016
TBPT,,16772,1.8589
TBPT,,19093,1.9053
TBPT,,21423,1.9443
TBPT,,23755,1.979
TBPT,,26087,2.01
TBPT,,28411,2.0377
TBPT,,30743,2.0624
TBPT,,33074,2.0848
TBPT,,35410,2.1047
TBPT,,37736,2.1224
TBPT,,40068,2.1385
TBPT,,42401,2.1531
TBPT,,44731,2.1656
TBPT,,49394,2.1902
TBPT,,51719,2.2014
TBPT,,54052,2.2124
TBPT,,56390,2.2229
TBPT,,58716,2.2325


   K,1,0,-2,0
K,2,0,2,0
K,3,.2,2,0
K,4,.2,-2,0
K,5,.2,-1,0
K,6,.2,1,0
K,7,.21,2,0
K,8,.21,-2,0
K,9,.21,-1,0
K,14,.21,1,0
K,15,.39,-2,0
K,16,.39,2,0
K,17,.4,-2,0
K,18,.4,2,0
K,19,.4,-.05,0
K,20,.4,.05,0
K,21,.45,.05,0
K,22,.45,-.05,0
K,23,1.2,-2,0
K,24,1.2,2,0
K,25,.21,-.5,0
K,26,.21,-.5,0
K,27,.21,.5,0
```

```
K,28,.21,.5,0
K,31,.21,.003,0
K,33,.21,-.003,0
K,32,.207,0,0
K,41,.21,.006,0
K,42,.21,-.006,0



   A,1,2,3,6,5,4
A,4,5,9,8
A,5,6,14,41,31,32,33,42,9
A,6,3,7,14
A,8,9,42,33,32,31,41,14,7,18,20,19,17
A,19,20,21,22
A,17,19,22,21,20,18,24,23
nummrg,all
/pnum,area,1
/replot
aplot

L,31,33

MP,murx,4,1

ASEL,s,area,,1,1
AATT,1
ASEL,s,area,,2,2
AATT,1
ASEL,s,area,,3,3
AATT,2
ASEL,s,area,,4,4
AATT,1
ASEL,s,area,,5,5
AATT,1
ASEL,s,area,,6,6
AATT,4
ASEL,s,area,,7,7
AATT,1
ASEL,all

   ESIZE,0.01
LESIZE,4,,,7100,,,,,1
LESIZE,11,,,4550,,,,,1
LESIZE,12,,,90,,,,,1
LESIZE,13,,,90,,,,,1
LESIZE,14,,,90,,,,,1
LESIZE,15,,,90,,,,,1
LESIZE,16,,,4550,,,,,1
LESIZE,30,,,250,,,,,1


   LESIZE,21,,,40,,,,,1

   AMESH,all


   BFA,6,JS,,,12000000

   FINISH

   /solu
solve
FINISH

/post1
Path,med,2,,1000
ppath,1,,.2105,-.005
ppath,2,,.2105,.005
pdef,,b,sum,avg
pdef,,b,x,avg
pdef,,b,y,avg

Path,med5,2,,1000
ppath,1,,.2105,-.005
ppath,2,,.2105,.005
pdef,,b,sum,avg
pdef,,b,x,avg
pdef,,b,y,avg

Path,med4,2,,1000
```

```
ppath,1,,.2104,-.005
ppath,2,,.2104,.005
pdef,,b,sum,avg
pdef,,b,x,avg
pdef,,b,y,avg

Path,med3,2,,1000
ppath,1,,.2103,-.005
ppath,2,,.2103,.005
pdef,,b,sum,avg
pdef,,b,x,avg
pdef,,b,y,avg

Path,med2,2,,1000
ppath,1,,.2102,-.005
ppath,2,,.2102,.005
pdef,,b,sum,avg
pdef,,b,x,avg
pdef,,b,y,avg

Path,med1,2,,1000
ppath,1,,.2101,-.005
ppath,2,,.2101,.005
pdef,,b,sum,avg
pdef,,b,x,avg
pdef,,b,y,avg


    Path,med001,2,,1000
ppath,1,,.21001,-.005
ppath,2,,.21001,.005
pdef,,b,sum,avg
pdef,,b,x,avg
pdef,,b,y,avg
```

Appendix D

Wavelet Analysis for MFL Radial Signal

This code was designed for Matlab platform. This program will compute a wavelet analysis for a given 1-D signal.

```
    s = Brad;
l_s = length(s);

[cA1, cD1]= dwt(s,'haar');

A1 = upcoef('a', cA1,' haar', 1, l_s);
D1 = upcoef('d', cD1,' haar', 1, l_s);

[cA2, cD2] = dwt(cA1,' haar');
[cA3, cD3] = dwt(cA2,' haar');
[cA4, cD4] = dwt(cA3,' haar');
[cA5, cD5] = dwt(cA4,' haar');
[cA6, cD6] = dwt(cA5,' haar');
[cA7, cD7] = dwt(cA6,' haar');
[cA8, cD8] = dwt(cA7,' haar');

A8 = upcoef('a', cA8,' haar', 8, l_s);
D1 = upcoef('d', cD1,' haar', 1, l_s);
D2 = upcoef('d', cD2,' haar', 2, l_s);
D3 = upcoef('d', cD3,' haar', 3, l_s);
D4 = upcoef('d', cD4,' haar', 4, l_s);
D5 = upcoef('d', cD5,' haar', 5, l_s);
D6 = upcoef('d', cD6,' haar', 6, l_s);
D7 = upcoef('d', cD7,' haar', 7, l_s);
D8 = upcoef('d', cD8,' haar', 8, l_s);

figure(100)
subplot(10,1,1);plot(s)
subplot(10,1,2);plot(A8)
subplot(10,1,3);plot(D8)
subplot(10,1,4);plot(D7)
subplot(10,1,5);plot(D6)
subplot(10,1,6);plot(D5)
subplot(10,1,7);plot(D4)
subplot(10,1,8);plot(D3)
subplot(10,1,9);plot(D2)
subplot(10,1,10);plot(D1)

figure(108)
plot(s)
hold on
plot(A8+D8+D7+D6+D5+D4+D3+D2+D1,'r')
```

Bibliography

[1] H. G. C. Sidney Burrus, Ramesh A. Gopinath, *Introduction to Wavelets and Wavelet Transforms.* Prentice Hall, 1998.

[2] D. E. Bray and R. K. Stanley, *Nondestructive Evaluation: A Tool in Design, Manufacturing, and Service.* CRC Press, 1997.

[3] Y. . T. M. Enokizono and T. Chady, "Crack size and shape determination by moving magnetic field type sensor," *IEEE Transactions on Magnetics*, vol. 34, pp. 1252–1254, July 1998.

[4] F. Förster, "New findings in the field of non-destructive magnetic leakage field inspection," *NDT International*, vol. 19, pp. 3–14, February 1986.

[5] G. Y. T. Yong Li, John Wilson, "Experiment and simulation study of 3d magnetic field sensing for magnetic flux leakage defect characterisation," *NDT and E International*, 2006.

[6] H. W. F. Sung and C. rudowicz, "A closer look at the hysteresis loop for ferromagnets," 2002.

[7] C. Mandache and L. Clapham, "A model for a magnetic flux leakage signal predictions," *Journal of Physics D: Applied Physics*, 2003.

[8] S. M. Dutta, *Magnetic Flux Leakage Sensing: The Forward and Inverse Problems.* PhD thesis, Rice University, 2008.

[9] R. R. David Halliday, *Physics.* Wiley, 1962.

[10] J. A. Edminister, *Electromagnetics.* Schaum's Outlines, 1993.

[11] R. Bozorth and D. Chapin, "Demagnetizing factors of rods," *Journal of Applied Physics*, 1942.

[12] J. Maxwell, *A Treatise on Electricity and Magnetism*, vol. II. Drover, third edition ed., 1891.

[13] L. E. M. Tejedor, H. Rubio and R. Iglesias, "External fields created by uniformly magnetized ellipsoids and spheroids," *IEEE Transactions on Magnetics*, vol. 31, pp. 830–836, January 1995.

[14] J. Hwang and W. Lord, "Finite element modeling of magnetic field/defect interactions," *ASTM Journal of Testing and Evaluation*, vol. 3, no. 1, pp. 21–25, 1975.

[15] D. Atherton and W. Czura, "inite element calculations on the effects of permeability variation on magnetic flux leakage signals," *NDT International*, vol. 20, pp. 239–241, August 1987.

[16] D. Atherton and M. Daly, "Finite element calculation of magnetic flux leakage detector signals," *NDT International*, vol. 20, pp. 235–238, August 1987.

[17] T. Roberts, "Finite element analysis of magnetic flux leakage in coiled tubing," Master's thesis, The University of Tulsa, 2003.

[18] W. C. Breidenthal, "Comparison of experimental measurments and 2d magnetostatic finite element calculations of magnetic flux leakage in steel coiled tubing," Master's thesis, The University of Tulsa, 2005.

[19] A. J. Lynch, *Magnetic Flux Leakage Robotic Pipe Inspection: Internal and External Methods.* PhD thesis, Rice University, 2009.

[20] G. O. J.-M. P. Michel Misiti, Yves Misiti, *Wavelets and their Applications.* Iste, 2007.

[21] L. Debnath, *Wavelet Transforms and Their Applications.* Birkhäuser, 2002.